A three-dimensional, multinutrient, and size-structured ecosystem model for the North Atlantic

Ivan D. Lima and Scott C. Doney

Department of Marine Chemistry and Geochemistry, Woods Hole Oceanographic Institution, Woods Hole, Massachusetts, USA

Received 10 September 2003; revised 12 March 2004; accepted 29 June 2004; published 21 September 2004.

[1] We incorporate multinutrient and size-structured ecosystem dynamics into a three-dimensional ocean general circulation model for the North Atlantic. The model reproduces the magnitude and general spatial and temporal patterns in nutrients, chlorophyll and primary production seen in in situ (BATS, NABE, and OWSI) and satellite (SeaWiFS) data, showing substantial improvements over prior basin-scale simulations. Model skill is evaluated quantitatively against SeaWiFS data using a Taylor diagram approach. Model-data correlation R for the overall surface chlorophyll time-space distribution is $\sim$0.6, with comparable model and observed total variability. The agreement relative to satellite-based primary production is somewhat weaker ($0.2 < R < 0.5$). The simulations capture observed ecological characteristics, e.g., the dominance of picoplankton and episodic diatom blooms in the subtropics, nutrient-controlled plankton succession at higher latitudes, and associated seasonal/depth changes in new and regenerated production and particle export. In a sensitivity experiment that mimics behavior of simpler single-species models, removal of diatom silica limitation leads to major shifts in community structure and export and larger model-data errors similar to previous model studies. Model results also suggest that episodic diatom blooms at BATS may be related to interannual variations in the southward transport of nutrients, mainly SiO_3, and plankton cells. *INDEX TERMS:* 4815 Oceanography: Biological and Chemical: Ecosystems, structure and dynamics; 4817 Oceanography: Biological and Chemical: Food chains; 4842 Oceanography: Biological and Chemical: Modeling; 4854 Oceanography: Biological and Chemical: Physicochemical properties; *KEYWORDS:* ecosystem model, North Atlantic, multinutrient, size-structure, silica limitation

Citation: Lima, I. D., and S. C. Doney (2004), A three-dimensional, multinutrient, and size-structured ecosystem model for the North Atlantic, *Global Biogeochem. Cycles*, *18*, GB3019, doi:10.1029/2003GB002146.

1. Introduction

[2] The need to quantify and project the ocean response to and feedbacks on anthropogenic perturbations has sparked a renewed interest in marine biogeochemical models the last decade [e.g., *Fasham et al.*, 1990; *Sarmiento et al.*, 1993; *Doney et al.*, 1996; *Doney*, 1999; *Dutkiewicz et al.*, 2001]. Most model implementations are based on comparatively simple trophic interactions with a few basic compartments: nutrients, phytoplankton, zooplankton and detritus (so called NPZD class of models). Nitrogen [*Fasham et al.*, 1990] or phosphorus [*Doveri et al.*, 1993] are used as natural ''currencies'', under the assumption that they are the limiting nutrients in marine systems. This pragmatic approach to the functional categorization of organisms largely ignores the taxonomic and biogeochemical diversity and food web complexities characteristic to such systems [*Pomeroy*, 1974]. Nevertheless, this class of bulk models provides a useful general framework to describe and analyze ecosystem functioning and facilitates the evaluation of such models against in situ chlorophyll and primary productivity measurements as well as satellite data.

[3] Recently, this traditional NPZD model framework has been expanded to include multielement nutrient limitation, distinct phytoplankton functional groups, and more realistic biogeochemistry. One-dimensional simulations have been used to investigate nutrient and carbon fluxes at individual sites [*Pondaven et al.*, 2000; *Hood et al.*, 2001] regionally [*Loukos et al.*, 1997; *Denman and Peña*, 1999; *Leonard et al.*, 1999] and globally [*Moore et al.*, 2002a, 2002b]. Multinutrient, size-structured ecosystem models based on fully three-dimensional time-dependent ocean general circulation models (OGCM) also have begun to appear in the literature [*Gregg*, 2002; *Christian et al.*, 2002a, 2002b; *Aumont et al.*, 2003]. In this study, we report results from a relatively complex ecosystem simulation in an OGCM for the North Atlantic.

Copyright 2004 by the American Geophysical Union.
0886-6236/04/2003GB002146$12.00

[4] The ecosystem component includes distinct phytoplankton functional groups, as well as size structure, and a mechanistic phytoplankton growth and photoadaptation model [*Geider et al.*, 1998] that accounts for multielement nutrient limitation (nitrogen and silica). Iron is not included in the model as it is typically not considered an important limiting nutrient in the North Atlantic [*Martin et al.*, 1993; *Fung et al.*, 2000] due to relatively strong mineral dust inputs from continents [*Tegen and Fung*, 1995; *Mahowald et al.*, 1999]. The potentially important effects of nitrogen fixation, calcification and phosphate limitation are also not considered in the present model and are the subject of forthcoming work.

[5] Model results are compared with in situ data (BATS, Ocean Weather Station India and NABE) and SeaWiFS imagery. After quantitatively evaluating model skill against observations, we use our model as a heuristic tool to explore the dynamics of the pelagic ecosystem in the North Atlantic. In particular, we investigate seasonal and geographical patterns in nutrient limitation and phytoplankton community composition and the resulting impacts on new, regenerated and total primary production and the export of organic carbon. We also compare our model results with those from two previous basin-scale model studies of the North Atlantic, a seven-compartment biogeochemical model [*Fasham et al.*, 1990] that includes ammonium, nitrate and suspended and sinking detritus, into a coarse-resolution (2°) OGCM [*Sarmiento et al.*, 1993; *Fasham et al.*, 1993] and a very simple four-compartment (NPZD) model embedded in a eddy-permitting (1/3°) OGCM [*Oschlies et al.*, 2000; *Oschlies*, 2001, 2002]. The present work differs in that it combines a fairly complex and realistic ecosystem model with an intermediate resolution (0.8°) OGCM. Model-model comparison is complicated by the fact that each model uses a different OGCM and biogeochemical formulation. Nevertheless, by comparing results from such diverse models one can identify common strengths and deficiencies and gain insight into the basic features that are necessary to simulate ocean biology realistically.

2. Methods

2.1. Physical Model

[6] The physical component is the Los Alamos Parallel Ocean Program (POP) [*Smith et al.*, 1992], a three-dimensional, primitive equation numerical ocean model that uses a level-coordinate system and has an implicit free surface treatment of the barotropic equations [*Dukowicz and Smith*, 1994]. The model domain comprises the Atlantic Ocean from 19.6°S to 72.5°N and 98°W to 16.8°E, including the Gulf of Mexico and the western part of the Mediterranean Sea. The horizontal mesh is a Mercator grid with resolution of $\Delta\lambda = 0.8°$ and $\Delta\phi = 0.8°\cos\phi$, where λ and ϕ are longitude and latitude, respectively. Thus horizontal resolution varies from 88.9 km at the equator to 26.7 km at the northern boundary. The vertical grid has 40 nonuniform vertical levels that vary in thickness from approximately 10 m at the surface to 250 m at depth. The topography is derived from the ETOPO5 database and interpolated to the 0.8° grid. The depth at each horizontal grid point is set equal to that of the nearest vertical level in the model.

[7] A Laplacian operator is used for horizontal mixing of momentum. The horizontal mixing of tracers is done using the [*Gent and McWilliams*, 1990] parameterization, which forces the mixing to take place along isopycnal surfaces, thus avoiding spurious horizontal diapycnal mixing across sloping isopycnals. The viscosity and diffusivity coefficients vary spatially with the cube of the horizontal grid spacing with values of 5×10^7 and 6×10^6 cm^2 s^{-1} at the equator, respectively. The vertical viscosities and diffusivities are computed using the KPP mixing parameterization [*Large et al.*, 1994] with background values of 1.0 and 0.1 cm^2 s^{-1}, respectively. The KPP model includes parameterizations for mixing due to internal wave breaking, shear instability and double diffusion [*Large et al.*, 1994].

[8] The physical model is forced with daily wind stresses, derived from ECMWF TOGA Global Surface Analysis for the years 1985–1992, linearly interpolated to each model time step. The surface heat flux is computed using the ECMWF heat flux analysis of [*Barnier et al.*, 1995], arranged in restoring form, using monthly mean climatologies of sea surface temperature, an ice mask and net downward short-wave radiation. An effective net freshwater flux is simulated by restoring the surface salinity to the monthly [*Levitus et al.*, 1994] climatology using a 1-month restoring timescale. At the northern, southern, and eastern boundaries there is a 3° wide buffer zone where temperature and salinity are restored full depth to seasonal NODC climatology [*Levitus et al.*, 1994; *Levitus and Boyer*, 1994] with a restoring constant $1/\tau$ that varies linearly from 1/15 d^{-1} at the boundary to 0 d^{-1} at the interior end of the buffer zone.

2.2. Ecosystem Model

[9] The ecosystem component has eight basic compartments: two phytoplankton species (picophytoplankton P_1 and diatoms P_2), two classes of detritus (small/suspended D_1 and large/sinking D_2), zooplankton (Z), and the nutrients nitrate (NO_3^-), ammonium (NH_4^+) and silicate (SiO_3). The biotic and detrital compartments contain multiple elemental pools to track the flow of nitrogen, carbon and silica through the ecosystem (total of 17 ecological state variables). The structural relationship among the different compartments in the model is outlined in Figure 1. The general form of the time rate of change equations in terms of nitrogen are:

$$\frac{D(P_1)}{Dt} = U_1\left(I_{par}, T, NH_4, NO_3\right) P_1 - G(P_1)\, Z - e_1\, P_1 - s_1\, P_1^2 \tag{1}$$

$$\frac{D(P_2)}{Dt} = U_2\left(I_{par}, T, NH_4, NO_3, SiO_3\right) P_2 - G(P_2)\, Z - e_2\, P_2 - s_2\, P_2^2 \tag{2}$$

$$\frac{D(Z)}{Dt} = a\, G(P_1, P_2)\, Z - c\, Z - d\, Z^2 \tag{3}$$

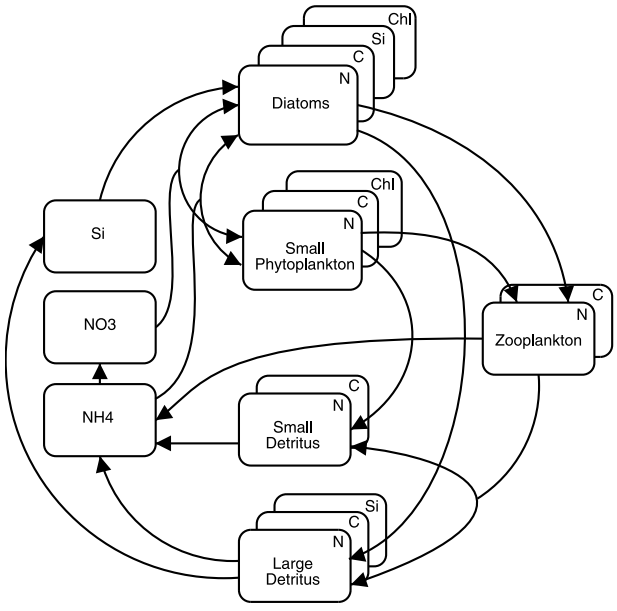

Figure 1. General structure of ecosystem model. The model's 17 state variables comprise the three nutrient compartments and the elemental pools in each main biological compartment.

$$\frac{D(D_1)}{Dt} = e_1 P_1 + s_1 P_1^2 + (1-\delta)\left(c Z + d Z^2\right) + (1-\lambda)(1-a) \cdot G(P_1, P_2) Z - r_1 D_1 \quad (4)$$

$$\frac{D(D_2)}{Dt} = e_2 P_2 + s_2 P_2^2 + \delta\left(c Z + d Z^2\right) - r_2 D_2 - w \frac{\partial D_2}{\partial z} \quad (5)$$

$$\frac{D(NO_3)}{Dt} = n\left(I_{par}\right) NH_4 - U_1\left(I_{par}, T, NH_4, NO_3\right) P_1 - U_2 \cdot \left(I_{par}, T, NH_4, NO_3\right) P_2 \quad (6)$$

$$\frac{D(NH_4)}{Dt} = r_1 D_1 + r_2 D_2 + \lambda (1-a) G(P_1, P_2) Z - n\left(I_{par}\right) NH_4 - U_1\left(I_{par}, T, NH_4\right) P_1 - U_2\left(I_{par}, T, NH_4\right) P_2 \quad (7)$$

$$\frac{D(SiO_3)}{Dt} = r_2 D_2 \left[D_{2(Si)} : D_{2(N)}\right] - U_2\left(I_{par}, T, SiO_3\right) \cdot P_2 \left[P_{2(Si)} : P_{2(N)}\right] \quad (8)$$

The phytoplankton, zooplankton and detritus source and sink terms are converted to carbon fluxes by multiplication with the respective carbon to nitrogen ratio ([C:N]) computed in the model. Parameter values and definitions are given in Table 1.

[10] Phytoplankton growth and photoadaptation $U_i(I_{par}, T, NH_4, NO_3)$ are computed following a modified version of the growth model of *Geider et al.* [1998] (hereinafter referred to as GD98). Environmental factors irradiance (I_{par}), nutrients and temperature determine the instantaneous rates of light utilization, carbon and nutrient assimilation and chlorophyll synthesis. These instantaneous rates are then modulated by the effects of past environmental conditions through time-evolving intracellular quotas [Chl:C] and [N:C]. The GD98 model was modified for the present study to allow for two nitrogen sources (NO_3^- and NH_4^+) and for growth limitation by the [Si:C] quota for diatoms, in a similar manner as for nitrogen. Maximum and minimum cell quotas for each nutrient are input parameters (Table 1). Phytoplankton [N:C] ratios are taken from GD98, and the [Si:C] diatom cell quota is found by multiplying the GD98 [N:C] values by an average [Si:N] ratio for larger diatoms (1.2) [*Brzezinski*, 1985]. We use a maximum [Chl:N] ratio of 2.5 mg Chl (mMol N)$^{-3}$ that is well within the range reported by *Geider et al.* [1997]. The generic form of the photosynthetic, nutrient uptake and photoadaptation rates computed in U_i for one limiting nutrient (N) are:

$$\frac{1}{C}\frac{dC}{dt} = P^C_{\max}\left[1 - e^{\frac{-\alpha\,\theta^C I_{par}}{P^C_{\max}}}\right] - \zeta V^N_C; \quad \frac{1}{N}\frac{dN}{dt} = \frac{V^N_C}{Q}; \quad \frac{1}{Chl}\frac{dChl}{dt} = \frac{\rho_{Chl} V^N_C}{\theta^C} \quad (9)$$

where the maximum photosynthetic rate $P^C_{\max}$ and carbon-specific nutrient uptake rate V^N_C are given by:

$$P^C_{\max} = P^C_{ref}\left[\frac{Q - Q_{\min}}{Q_{\max} - Q_{\min}}\right] T_f; \quad V^N_C = V^N_{ref}\left[\frac{Q - Q_{\min}}{Q_{\max} - Q_{\min}}\right] \quad T_f\left(\frac{N}{N + K_N}\right) \quad (10)$$

T_f is the temperature response function, Q is the phytoplankton [N:C] ratio, ζ represents the cost of biosynthesis, θ^C is the phytoplankton [Chl:C] ratio and ρ_{Chl} is a dimensionless chlorophyll synthesis regulation term given by:

$$\rho_{Chl} = \theta^N_{\max}\frac{P^C_{\max}}{\alpha\,\theta^C I_{par}}\left[1 - e^{\frac{-\alpha\,\theta^C I_{par}}{P^C_{\max}}}\right] \quad (11)$$

[11] The light intensity available for photosynthesis (I_{par}) at depth (z) is given by:

$$I_{par} = I_0\,\phi\, e^{-(\kappa_w + \kappa_{chl}(Chl_1 + Chl_2)))z} \quad (12)$$

where I_0 is the total irradiance at the surface, ϕ is the fraction of total irradiance that is available for photosynthesis (PAR), κ_w and κ_{chl} are the light attenuation coefficients due to water and phytoplankton self-shading, respectively, and Chl_1 and Chl_2 are the small phytoplankton and diatom chlorophyll concentrations. The diurnal cycle of light intensity is not considered for consistency with the forcing in the physical model, and I_0 is set to the temporally interpolated value of incoming short-wave radiation (W m^{-2}).

[12] Total nitrogen (NO_3^- + NH_4^+) uptake by the phytoplankton and the inhibiting effect of NH_4^+ concentration on

Table 1. Parameter Values and Definitions for the Ecosystem Model

Parameter	Value	Units	Definition	Source[a]
ϕ	0.45		PAR fraction of total irradiance	
α	0.25	mMol C (mg Chl)$^{-1}$ d^{-1} m^2 W^{-1}	initial slope of the $P-I$ curve	1
κ_w	0.04	m^{-1}	light attenuation coefficient	
κ_{chl}	0.035	m^2 (mg Chl)$^{-1}$	phytoplankton self-shading coefficient	2
T_{ref}	30	°C	reference temperature	
P^C_{ref}	3.0	d^{-1}	phytoplankton maximum C-specific growth rate	1
θ^N_j	2.5	mg Chl (mMol N)$^{-1}$	phytoplankton maximum Chl:N ratio	1
Q^N_{min}	0.034	mol N (mol C)$^{-1}$	phytoplankton minimum N:C ratio	1
Q^N_{max}	0.170	mol N (mol C)$^{-1}$	phytoplankton maximum N:C ratio	1
Q^{Si}_{min}	0.041	mol Si (mol C)$^{-1}$	diatom minimum Si:C ratio	3
Q^{Si}_{max}	0.204	mol Si (mol C)$^{-1}$	diatom maximum Si:C ratio	3
$V^N_{C\ ref}$	0.51	mMol N (mMol C)$^{-1}$ d^{-1}	C-specific N uptake rate at T_{ref}	1
$V^{Si}_{C\ ref}$	$P^C_{ref} \times Q^{Si}_{max}$	mMol Si (mMol C)$^{-1}$ d^{-1}	C-specific Si uptake rate at T_{ref}	
R_{ref}	0.0	d^{-1}	respiration/degradation at T_{ref}	1
ζ	2.33	mMolC mMolN^{-1}	cost of of biosynthesis	1
$K_1^{NO_3}$	0.60	mMol N m^{-3}	NO_3^- half saturation constant for picophytoplankton	
$K_1^{NH_4}$	0.007	mMol N m^{-3}	NH_4^+ half saturation constant for picophytoplankton	
$K_2^{NO_3}$	1.5	mMol N m^{-3}	NO_3^- half saturation constant for diatoms	
$K_2^{NH_4}$	0.07	mMol N m^{-3}	NH_4^+ half saturation constant for diatoms	
$K_2^{SiO_3}$	1.10	mMol N m^{-3}	silicate half saturation constant for diatoms	4
e_1	0.1	d^{-1}	picophytoplankton respiration rate	5
e_2	0.1	d^{-1}	diatom respiration rate	5
s_1	0.1	[mMol N m^{-3} d]$^{-1}$	picophytoplankton aggregation rate	5
s_2	0.1	[mMol N m^{-3} d]$^{-1}$	diatom aggregation rate	5
g_1	3.25	d^{-1}	zooplankton maximum growth rate when grazing picophytoplankton	6
g_2	2.75	d^{-1}	zooplankton maximum growth rate when grazing diatoms	6
K_Z	0.75	mMol N m^{-3}	half saturation constant for zooplankton grazing	
c	0.1	d^{-1}	zooplankton respiration rate	7
d	0.25	[mMol N m^{-3} d]$^{-1}$	zooplankton mortality rate	
a	0.7		zooplankton assimilation efficiency	8
λ	0.5		zooplankton egestion allocation factor	
r_1	0.2	d^{-1}	remineralization rate for small detritus	9
r_2	0.2	d^{-1}	remineralization rate for large detritus	9
n	0.1	d^{-1}	nitrification rate	6
w	25	m d^{-1}	large detritus sinking rate	10

[a]Sources are as follows: 1, *Geider et al.* [1998]; 2, *Fasham et al.* [1990]; 3, *Brzezinski* [1985] and *Geider et al.* [1998]; 4, *Brzezinski and Nelson* [1989], *Nelson and Tréguer* [1992], and *Nelson et al.* [2001]; 5, *Franks et al.* [1986], *Wroblewski* [1989], *Fasham et al.* [1990], and *Doney et al.* [1996]; 6, *Moore et al.* [2002a, 2002b]; 7, *Harrison* [1980, 1992] and *Bidigare* [1983]; 8, *Franks et al.* [1986]; 9, *Eppley and Peterson* [1979], *Harrison* [1980], *McCarthy and Carpenter* [1983], and *Harrison* [1992]; 10, *Smayda* [1969], *Fasham et al.* [1990], and *McCreary et al.* [1996].

NO_3^- uptake is modeled using the substitutive equation of *O'Neil et al.* [1989]. The half saturation constants for NH_4^+ and NO_3^- are set to relatively low and high values, respectively (Table 1), to give the phytoplankton a reasonably strong preference for NH_4^+. In a series of test runs, these values provided the best fit of the model to observations. Silica uptake by the diatoms is modeled using standard Michaelis-Menten kinetics. Half saturation for SiO_3 varies considerably among regions (0.5–4.6 mMol m^{-3}) [*Brzezinski and Nelson*, 1989; *Nelson and Tréguer*, 1992; *Nelson et al.*, 2001] and a medium value of 1.2 mMol m^{-3} is chosen.

[13] The single model zooplankton compartment is assumed to represent a diverse community of grazers, using a Holling type III predation functional response with different maximum growth/grazing rates for the zooplankton depending on the food source:

$$G(P_i) = g_i \frac{P_i^2}{P_i^2 + K_Z} \tag{13}$$

The grazing parameterization increases the overall stability of the system and simulates reasonably well the effects of size-dependent grazing on the phytoplankton community [*Armstrong*, 1999; *Lima et al.*, 2002]. A relatively high zooplankton quadratic mortality rate is used to increase model stability [*Steele and Henderson*, 1992; *Lima et al.*, 2002].

[14] The partitioning of zooplankton losses between the suspended and sinking detrital compartments depends on the type of food source and is parameterized in terms of an excretion allocation factor (δ):

$$\delta = \frac{0.3\,G(P_1) + 0.7\,G(P_2)}{G(P_1) + G(P_2)} \tag{14}$$

where $G(P_i)$ represents the Holling type III predation functional response for the phytoplankton species i (equation (13)). δ approaches 0.7 for $P_2 \gg P_1$. Thus, as the relative contribution of diatoms (P_2) to total grazing increases, a proportionally larger fraction of zooplankton excretion and mortality is directed to the large sinking detritus compartment.

[15] The NO_3^- compartment receives input from nitrification at light levels corresponding to those at the bottom of the euphotic zone (1% of surface I_{par}) and below. The temperature dependency of zooplankton growth rates and detrital remineralization rates is computed by multiplying

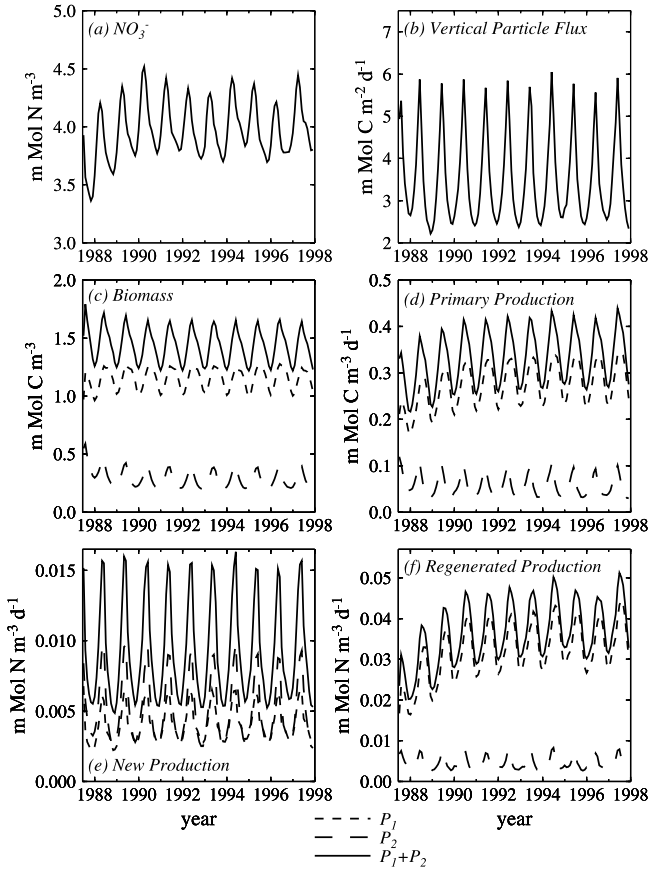

Figure 2. Time series of monthly means for the euphotic zone (107 m) average of (a) nitrate, (b) vertical particle flux at 107 m, (c) phytoplankton biomass, (d) total primary production, (e) new production, and (f) regenerated production for the picophytoplankton (P_1), diatoms (P_2), and total phytoplankton ($P_1 + P_2$).

the respective maximum instantaneous rates (Table 1) by the same temperature function (Arrhenius relation) used in the phytoplankton growth model (GD98).

2.3. Coupled Model Initialization and Integration Procedure

[16] All biogeochemical tracers are coupled into the model through the advection-diffusion equation:

$$\frac{\partial X}{\partial t} + \vec{V} \cdot \nabla X - \nabla \cdot (\kappa \nabla X) = \frac{DX}{Dt} \tag{15}$$

where X represents each biogeochemical tracer and $\frac{DX}{Dt}$ the respective source-sink term in the biogeochemical model (equations (1)–(8)). A third-order upwind advection scheme is used for all tracers to avoid negative tracer values near sharp gradients with minimal implicit diffusion [*Hecht et al.*, 1998].

[17] The coupled model is initialized with the ocean at rest, temperature and salinity set equal to the June NODC climatology [*Levitus et al.*, 1994; *Levitus and Boyer*, 1994], and nitrate and dissolved silica from the annual mean NODC climatology [*Conkright et al.*, 1994]. All remaining biogeochemical compartments are initialized with a uniformly low value (0.1 mMol N m^{-3} or equivalent). The physical model is spun up for 2 years (1 June 1985 through 1 June 1987), driven by the ECMWF winds and the boundary forcing described above. The ecosystem model is then "switched on", and the integration continues for another 10.5 years (through 1 December 1997). Because of the relatively short integration time and our focus on the upper water column, the deep nitrate and silica fields are restored to their respective NODC annual means, with a restoring constant $1/\tau$ that varies linearly with depth from 0 d^{-1} at 400 m to 1/30 d^{-1} at 1100 m and remains constant for depths below that. The ecosystem model spins up rapidly and reaches an approximate repeating annual cycle after 2 years (Figure 2). The annual cycle does not repeat itself exactly because the model is forced with nonclimatological daily wind stresses.

2.4. Field and Satellite Data Sets

[18] Monthly climatological means of chlorophyll and primary productivity from the last 3 years of model integration are compared with estimates derived from SeaWiFS imagery. Surface chlorophyll data from monthly level 3 standard images covering the period from September 1997 to August 2003 were extracted for the model domain area and averaged and remapped to the model grid. Monthly primary productivity is estimated from SeaWiFS chlorophyll data using the VGPM model of *Behrenfeld and Falkowski* [1997]. Model skill is evaluated quantitatively against satellite estimates of chlorophyll and primary productivity using a Taylor diagram [*Taylor*, 2001], a two-dimensional plot comparing the total variance and space/time correlation between a test (model) and a reference (satellite) field. Four types of comparisons are made using different subsets of model and and satellite fields to explore how well the model does in replicating different aspects of the observed variability. The model and observed standard deviation and correlation are computed, respectively: for the sum of all 12 months and all model grid points (total space-time); for each month individually (monthly-spatial); for monthly anomalies from the local annual mean (monthly-time); and for the annual mean (spatial-annual). For a more detailed description of the Taylor diagram and the statistics and computations involved see the Appendix section. Oceanic bio-optical variability follows approximately a lognormal distribution [*Campbell*, 1995] so the natural log transformation is applied to the chlorophyll and primary productivity fields prior to the analysis.

[19] Observations from two time series stations, the Bermuda Atlantic Time series Study (BATS, 31°49′N, 64°09′W) [*Michaels and Knap*, 1996; *Steinberg et al.*, 2001] and Ocean Weather Station India (OWSI, 59°N, 18°W) [*Williams and Robinson*, 1973] and from one process oriented study, the North Atlantic Bloom Experiment (NABE, 47°N, 20°W) [*Weeks et al.*, 1993] are compared with model output from the corresponding grid points in the model domain. Because of the relative scarcity of data at

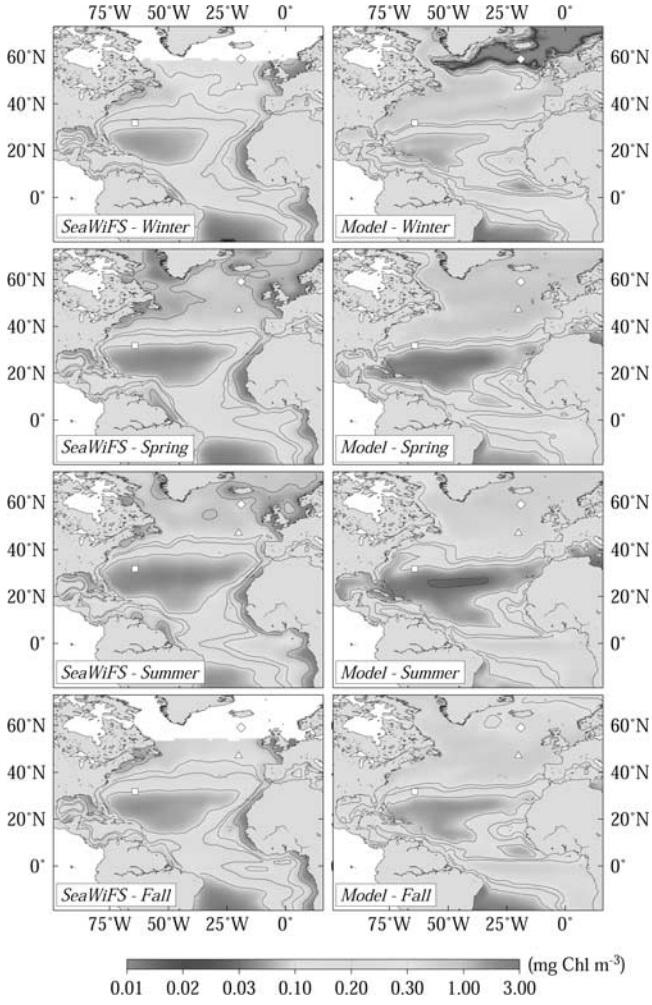

Figure 3. Seasonal climatologies of surface chlorophyll concentrations (mg Chl m^{-3}) from the last 3 years of model integration and SeaWiFS imagery (October 1998 to September 1999). White symbols represent the location of the BATS (squares), NABE (triangles), and OWSI (diamonds) sites. See color version of this figure at back of this issue.

this site, the NABE data include observations from the US JGOFS cruises, the Plankton Biogeochemical Ocean Flux Study (BOFS) [*Lowry et al.*, 1994] and the Plankton Reactivity in the Marine Environment (PRIME) [*Hadziabdic and Cramer*, 1999]. For each site, all available observations on nutrients, chlorophyll and primary production were grouped by month and depth intervals to produce monthly average profiles.

[20] Model results on the relative abundance of the different phytoplankton groups are presented in chlorophyll units to facilitate comparison with available observations on community structure, which are usually reported in terms of pigment concentrations. Because of the scarcity of depth-resolving records of zooplankton abundance and the highly parameterized nature of the model's zooplankton compartment, we do not attempt to make direct comparisons of modeled zooplankton abundance and distribution with observations.

3. Basin-Scale Surface Chlorophyll and Primary Production

[21] The model reproduces the observed large-scale geographical and seasonal patterns of surface chlorophyll distribution and primary productivity derived from SeaWiFS imagery (Figures 3 and 4). Agreement in the subtropics is particularly good in the fall and winter. In the spring and summer, however, simulated subtropical chlorophyll levels are noticeably lower than observed, and the oligotrophic region is expanded over a larger area. Still, minimum modeled chlorophyll concentrations in the oligotrophic gyre (0.019 mg Chl m^{-3}) during spring and summer are relatively close to the lowest satellite values (0.037 mg Chl m^{-3}). The lowest simulated primary production values

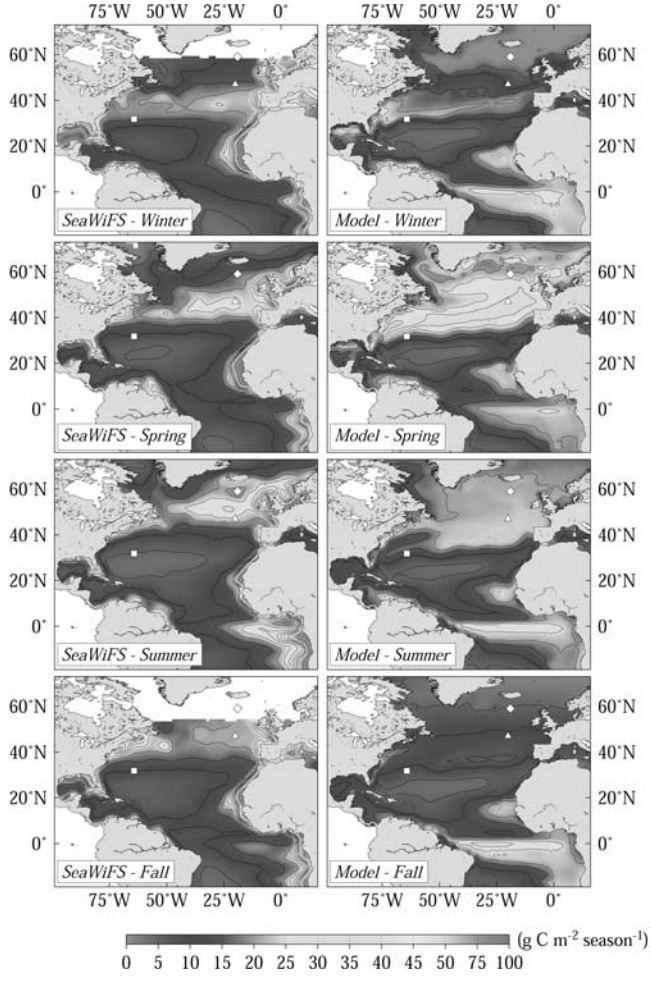

Figure 4. Seasonal climatologies of primary productivity estimates (g C m^{-2} $season^{-1}$) from the last 3 years of model integration and from SeaWiFS chlorophyll data using the VGPM model of *Behrenfeld and Falkowski* [1997]. White symbols represent the location of the BATS (squares), NABE (triangles), and OWSI (diamonds) sites. See color version of this figure at back of this issue.

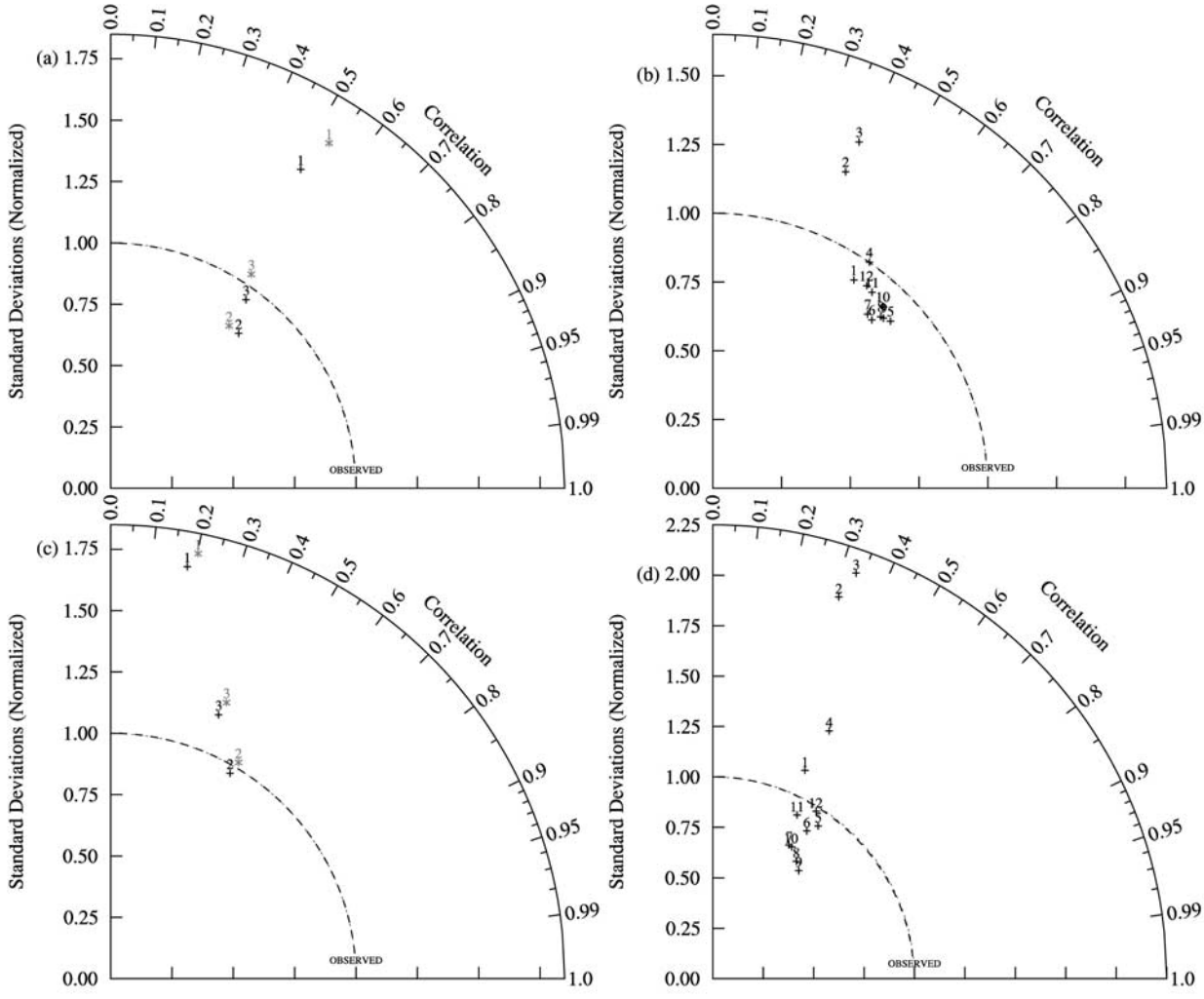

Figure 5. Taylor diagram comparing monthly climatological fields of log transformed surface chlorophyll estimates (mg Chl m^{-3}) from the model and satellite and monthly primary productivity estimates (g C m^{-2} $month^{-1}$) from the model and satellite data using the VGPM model of *Behrenfeld and Falkowski* [1997]. The radial distances from the origin are proportional to the ratio of the model and satellite standard deviations and the azimuthal positions correspond to the correlation between the model and satellite fields. The distances from the model points to the satellite point are proportional to the normalized RMS difference between the fields (Table 2). Black points represent the main run, and red points represent the ''no silica limitation'' run (NSLIM). (a) Chlorophyll monthly-time (1), spatial-annual (2), and total time-space (3) statistics. (b) Chlorophyll monthly-spatial statistics. (c) Primary productivity monthly-time (1), spatial-annual (2), and total time-space (3). (d) Primary productivity monthly-spatial statistics. Numbers in Figure 5b and 5d correspond to the months of the year. See color version of this figure at back of this issue.

in the subtropical gyre also occur during spring and summer and are ~50% lower than satellite derived estimates.

[22] The circulation model overestimates the winter mixed layer depth along the northwestern edge of the subtropical gyre by more than 150 m. The deep convection entrains an excess of nutrients that leads to an overestimation of surface chlorophyll and primary production along the northern flank of the subtropical gyre during winter and spring by ~60% (Figures 3 and 4). High chlorophyll values are also advected northward and eastward by the Gulf Stream and North Atlantic Current, causing positive anomalies at high latitudes in winter and fall (Figure 3). In their eddy-permitting simulations, *Oschlies et al.* [2000] also report a similar problem that persisted despite changes in the parameterization of vertical turbulent mixing [*Oschlies and Garçon*, 1999].

[23] Because of its spatial resolution, the model does not capture coastal processes very well. Most of the high chlorophyll and primary production values observed on the northeast coast of South and North America and the upwelling regions off the coast of Africa have counterparts in the model, although weaker ones. The model also over-

Table 2. Normalized RMS Difference of Log Transformed Surface Chlorophyll and Monthly Primary Productivity Estimates From the Model and SeaWiFS Imagery for the Three Different Cases Presented in Figures 5a and 5c

	Main Run	NSLIM Run
Chlorophyll, mg Chl m^{-3}		
Monthly-time case	1.354	1.425
Spatial-annual case	0.815	0.861
Total time-space case	0.912	0.967
Primary productivity, g C m^{-2} $month^{-1}$		
Monthly-time case	1.223	1.258
Spatial-annual case	1.199	1.223
Total time-space case	1.200	1.232

estimates chlorophyll concentrations and primary production along the equatorial upwelling region, a result of high the equatorial upwelling due to the closed southern boundary [*Smith et al.*, 2000] and the relatively high temperature-dependent phytoplankton growth rates in this region.

[24] Despite deficiencies, model-data correlation for the overall time-space distribution of satellite chlorophyll fields is ~0.6 and the magnitude of the model total time-space variability is comparable to the observed value (point 3 in Figure 5a; see also Table 2). The correlation for the annual mean spatial pattern (spatial-annual) is somewhat better while the correlation for the seasonal cycle (monthly-time) is somewhat worse (Figure 5a). The largest errors occur in late winter and early spring (February and March) and are directly related to the excess convections along the northern edge of the subtropical gyre described above (Figure 3). This difference is also reflected in the monthly-time statistics which show a higher amplitude of variation in the simulated seasonal cycle (point 1 in Figure 5a).

[25] Model performance in simulating monthly productivity (Figures 5c and 5d) is not as good as chlorophyll (Figures 5a and 5b). Modeled primary productivity is lower than the VGPM satellite estimated values over the most stratified and oligotrophic portion of the subtropical gyre (Figure 4) perhaps due to missing mesoscale nutrient inputs [*McGillicuddy et al.*, 2003]. The model also overestimates primary production along the northern edge of the subtropical gyre during winter and early spring and in the equatorial upwelling region (Figure 4). Thus the model generally overestimates the spatial and temporal amplitude of variation of the satellite estimates by 20% and 70%, respectively, with weaker correlations ($0.2 < R < 0.5$) (Figures 5c and 5d). Primary production algorithms vary widely in performance, and the best performing algorithms agree with in situ estimates within a factor of two [*Campbell et al.*, 2002]. Thus metrics of model skill will depend on the choice of primary production algorithm for the satellite reference field and may be lower as a result of deficiencies in the primary production algorithm used.

4. Annual Cycle at BATS

[26] There is generally good agreement between the observed and modeled annual cycles of surface chlorophyll (Figure 6a) and full depth NO_3^-, chlorophyll and primary production fields at BATS (Figure 7). However, the onset and peak of the spring bloom in the model occurs a month later than observed, and the model overestimates the magnitude of chlorophyll concentrations and primary production during the spring bloom by ~60% and ~25%, respectively (Figures 6a and 7c–7f). These discrepancies result because the modeled winter mixing is 80% deeper, has a shorter duration and is delayed relative to the observed climatological mean (Figure 7b). The intensity and timing of winter mixing at BATS show a fair amount of interannual variability [*Steinberg et al.*, 2001]. As a result, the climatological mean is is significantly shallower than the maximum in individual years, typically ~200–300 m [*Michaels and Knap*, 1996] similar to the model average. For the remainder of the seasonal cycle, however, modeled surface chlorophyll concentrations are higher (~15%) but closer to the range of observed values. Comparison with results from sensitivity runs show that the overestimation of chlorophyll concentrations in the DCML is also in part a result of excessive photoadaptation by the phytoplankton in the model. The suspended detritus → ammonium → picophytoplankton → micrograzer pathway with tight recycling under oligotrophic conditions allows the model to maintain primary production rates of ~0.4 mMol C m^{-3} d^{-1} at very low ambient NO_3^- concentrations (0.01 mMol N m^{-3}), which has proven to be very difficult with simpler ecosystem models [e.g., *Fasham et al.*, 1993; *Oschlies et al.*, 2000].

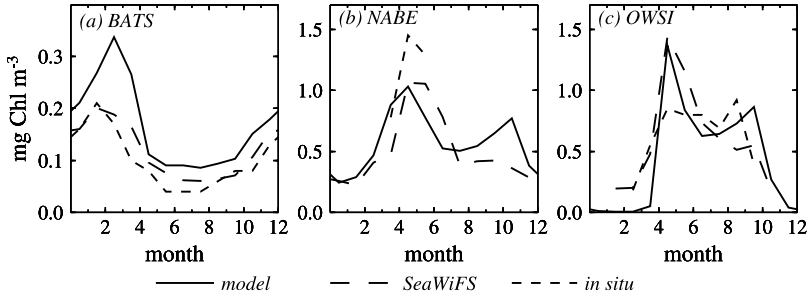

Figure 6. Time series of monthly climatological means of surface chlorophyll concentrations (mg Chl m^{-3}) from model, in situ observations, and SeaWiFS imagery (1998–1999) at the (a) BATS, (b) NABE, and (c) OWSI sites.

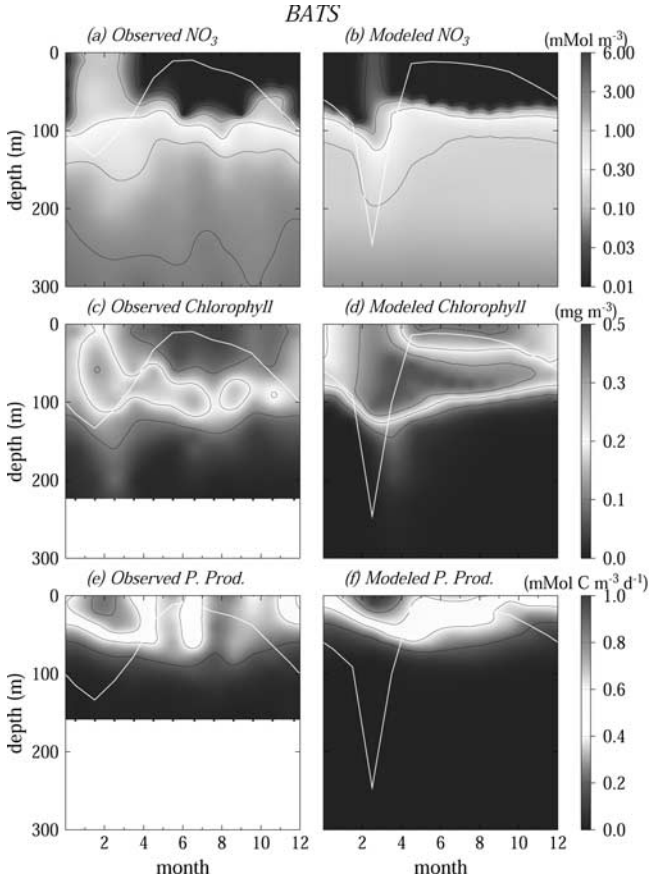

Figure 7. Time series of monthly climatological means of observed and modeled NO_3^- (mMol m^{-3}), chlorophyll concentrations (mg Chl m^{-3}), and primary production (mMol C m^{-3} d^{-1}) at the BATS site. White line represents mixed layer depth. See color version of this figure at back of this issue.

4.1. Community Dynamics

[27] Although both picophytoplankton and diatoms grow in response to the increased nitrate supply in late winter and early spring, the picophytoplankton dominate the bloom reaching maximum concentrations in March (Figure 8). Diatoms are significantly less abundant and reach maximum concentrations at depth (60–70 m) after the main bloom, in late spring and early summer. After the spring bloom, production in the upper part of the euphotic zone is mostly regenerated, while at depth, near the nutricline, nutrient supply (NO_3^-, SiO_3) is sufficient to maintain small but significant levels of new production in the DCML. These patterns are consistent with available observations at BATS [*Brzezinski and Nelson*, 1995; *Michaels and Knap*, 1996; *Nelson and Brzezinski*, 1997; *Steinberg et al.*, 2001; *DuRand et al.*, 2001].

4.2. Nutrient Limitation Patterns

[28] Simulated phytoplankton growth is limited by the nutrient with the lowest cell quota relative to its maximum. At BATS, nutrient entrainment in late winter allows both phytoplankton size classes to increase their nitrogen cell quotas (Figures 9a and 9b), with diatoms achieving near maximum silica cell quota. As spring progresses, both phytoplankton species become nitrogen limited, with diatoms more strongly limited because of their higher half saturation constant. By late spring and early summer, diatoms become severely silica limited and remain so throughout the rest of the seasonal cycle (Figure 9c), consistent with observations in the Bermuda region [*Brzezinski and Nelson*, 1995, 1996; *Nelson and Brzezinski*, 1997]. As found in field data [*Lessard and Murrell*, 1998], picophytoplankton abundance is controlled mainly by grazing.

4.3. Production and Export

[29] Model new and regenerated production peak at the same time (March) at BATS. New production drops to very low levels after April while regenerated production remains relatively high throughout the rest of the year (Figure 10b). The peak in the vertical particle flux corresponds to the maximum in the combination of diatom mortality and zooplankton excretion (not shown), which occur 1–2 months after the peak in primary production and chlorophyll (Figures 10a and 10b) due to the time lag associated with the zooplankton response and the timing of the diatom bloom (late spring, early summer). *Steinberg et al.* [2001] report a weak correlation between vertical particle flux and primary production at BATS with a time lag of one week. The significant contribution of diatoms to the formation of sinking organic matter at BATS (50–67%) is consistent with observations [*Brzezinski and Nelson*, 1995; *Nelson and Brzezinski*, 1997]. The magnitude of carbon particle flux (POC) in the summer (Figure 10b) is approximately 150% higher than those estimated from sediment traps, which have typical values of ~20 mg C m^{-2} d^{-1} at 150 m [*Michaels and Knap*, 1996; *Steinberg et al.*, 2001]. This discrepancy is certainly related to the overestimation of phytoplankton abundance in the model and biases as well as uncertainties associated with sediment trap measurements [*Steinberg et al.*, 2001].

5. Annual Cycle at NABE and OWSI

[30] At NABE, model results show good general agreement (Figure 11) with available in situ observations, mostly restricted to the spring bloom and early summer periods [*Weeks et al.*, 1993; *Lochte et al.*, 1993]. Modeled maximum surface chlorophyll concentrations during the bloom agree well with satellite estimates but are ~40% lower than in situ observations (Figure 6b). The onset and end of the spring bloom also occur a month earlier than in the in situ and satellite data, the difference possibly the result of deficiencies in the model's physical forcing. Numerical experiments with realistic forcing show that the onset of the North Atlantic spring bloom can vary by several weeks depending on surface heat and momentum fluxes [*Oschlies et al.*, 2000]. In our modeled time series, the fall bloom is stronger and occurs a month later than in the SeaWiFS derived climatology (Figure 6b). The modeled seasonal cycle is also consistent with current available knowledge

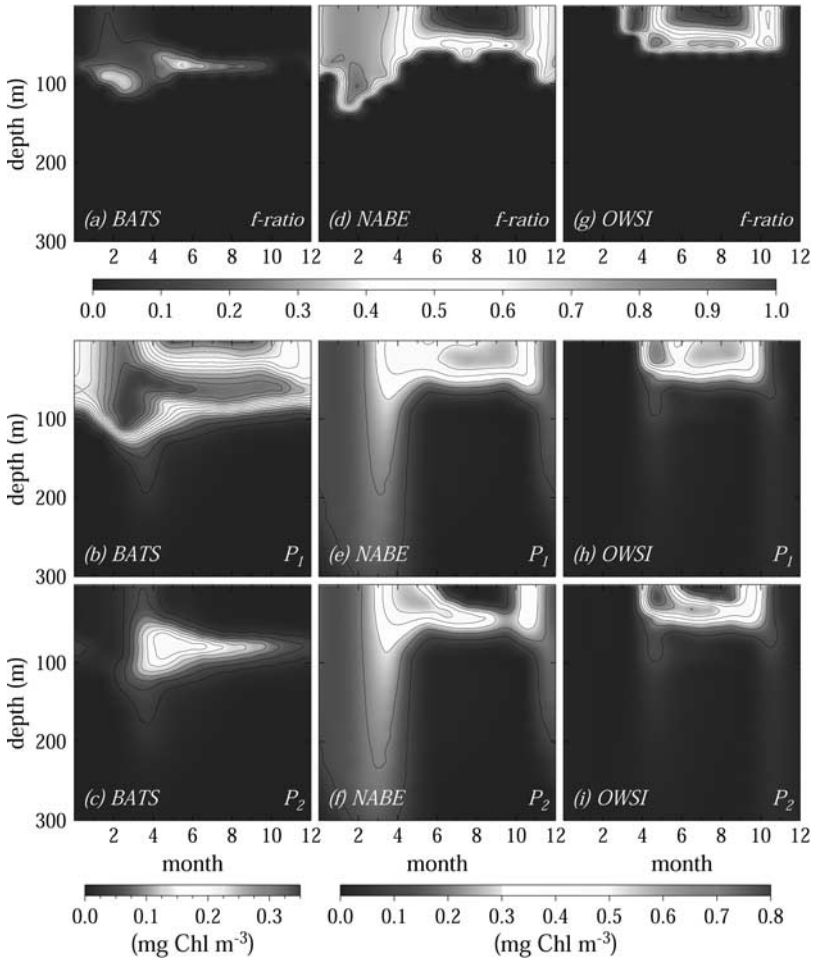

Figure 8. Time series of monthly climatological means of picophytoplankton (P_1) and diatoms (P_2) chlorophyll concentrations (mg m^{-3}) and *f* ratios as function of depth from the model at the locations corresponding to the (a–c) BATS, (d–f) NABE, and (g–i) OWSI sites. Note different color scale for BATS. See color version of this figure at back of this issue.

for this region of the ocean [*Mann and Lazier*, 1991; *Longhurst*, 1998]. Estimated winter NO_3^- concentrations [*Glover and Brewer*, 1988; *Garside and Garside*, 1993] are of the order of 10 mMol m^{-3}, comparable to model results (Figure 11b).

[31] OWSI data lack winter observations and vary in frequency but are commonly more frequent than monthly when available (Figures 6c and 12). The model fits the average annual cycle of the chlorophyll data remarkably well, with a seasonal cycle similar to that at NABE but shorter (Figure 12). However, maximum surface chlorophyll concentrations in the in situ observations are ~55% lower than satellite and model estimates and the in situ data do not show the sharp decline in chlorophyll over the summer seen in the satellite and model data (Figure 6c). The model reproduces the seasonal NO_3^- trend and the relatively high surface NO_3^- values observed during summer (2–3 mMol m^{-3}). However, nutrient and primary production measurements were relatively few and problematic (sometimes 2–3 observations per month), particularly at depth [*Williams and Robinson*, 1973; *Fasham et al.*, 1993].

5.1. Community Dynamics

[32] At NABE and OWSI, both phytoplankton groups grow rapidly in the spring reaching maximum concentrations near the surface (Figure 8) with diatoms comprising ~55% of the total phytoplankton biomass. After the spring bloom, phytoplankton levels decline, and the community near the surface transitions into a picophytoplankton dominated regime fueled by regenerated production, with significant levels of new production and diatom concentrations only in the DCML. This community shift is consistent with observations at NABE [*Sieracki et al.*, 1993; *Lochte et al.*, 1993]. The weaker fall bloom at NABE and OWSI is, in the most part, the result of an increase in diatom concentrations.

5.2. Nutrient Limitation Patterns

[33] At NABE and OWSI, both phytoplankton size classes are near their maximum cell quotas during the winter (Figure 9) as their growth (carbon fixation) is strongly light limited. The phytoplankton are also nitrogen-replete during the spring and summer months, as NO_3^- and NH_4^+ concentrations remain relatively high during this period (Figures 11 and 12). Diatoms are silica limited near the surface during

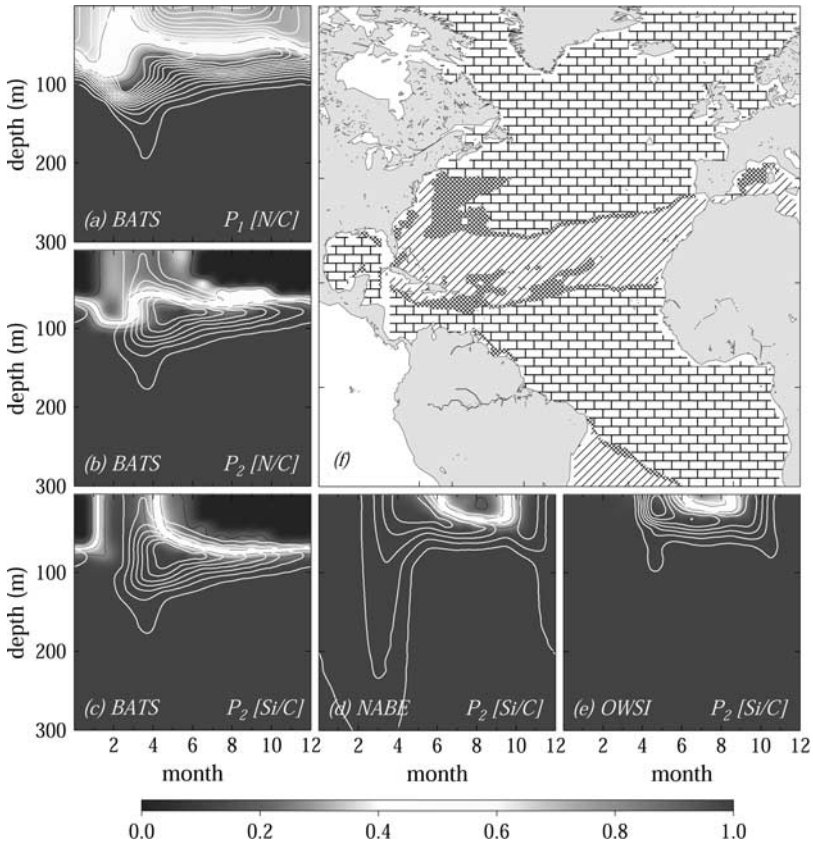

Figure 9. Time series of monthly climatological means of the picophytoplankton (P_1) and diatom (P_2) [N:C] and [Si:C] cell quotas relative to the respective maximum cell quotas as function of depth from the model at the locations corresponding to the (a–c) BATS, (d) NABE, and (e) OWSI sites. [N:C] and [Si:C] values below 0.2 near the surface in Figures 9b and 9c indicate $P_2 = 0$. White contour lines indicate picophytoplankton and diatom chlorophyll concentrations (mg m^{-3}) and correspond to the same contours in Figure 8. (f) Geographical nutrient limitation patterns for the diatoms averaged over the the euphotic zone (107 m). Rectangles indicate silica limitation, inclined lines indicate nitrogen limitation, and the cross-hatch pattern shows where the limiting nutrient varies seasonally. Symbols represent the location of the BATS (square), NABE (triangle), and OWSI (diamond) sites. See color version of this figure at back of this issue.

the summer months (Figure 9), leading to the demise of the diatoms in the upper layers (Figure 8) and the phytoplankton community shift noted above. The simulations are in excellent agreement with observations in the NABE region, where dissolved silicate depletion coincides with a shift in dominant phytoplankton from diatoms to small phytoplankton [*Sieracki et al.*, 1993; *Lochte et al.*, 1993].

5.3. Production and Export

[34] At NABE and OWSI, the peak in new production coincides with the spring bloom, while regenerated production reaches a maximum in early summer (Figures 10d and 10f). At both sites, the peak in the vertical particle flux occurs a month after the peak in new production and diatom abundance, and as at BATS is associated with the maximum in diatom mortality and zooplankton excretion (Figures 10d and 10f). The vertical particle flux minimum in late summer/early fall coincides with the minimum in diatom abundance (Figures 10c–10f) and a shift in community composition [*Buesseler et al.*, 1992; *Sieracki et al.*, 1993; *Lochte et al.*, 1993]. The modeled particulate organic carbon flux at 150 m in the spring at NABE (153.2 mg C m^{-2} d^{-1}) is approximately 30% higher than observed from sediment traps (117.6 mg C m^{-2} d^{-1}) [*Lochte et al.*, 1993], a result of uncertainties associated with both sediment trap measurements and model errors.

6. Effects of Silica Limitation on Ecosystem Dynamics

[35] In the model, euphotic zone (0–107 m) diatom growth is generally nitrogen limited in the subtropical gyre and silica limited at higher latitudes and in upwelling regions along the equator and the west coast of Africa (Figure 9f). There is a fair degree of seasonal variation between nitrogen limitation (late winter and early spring) and silica limitation (remainder of the year), mostly along the northwest side of the subtropical gyre near the BATS

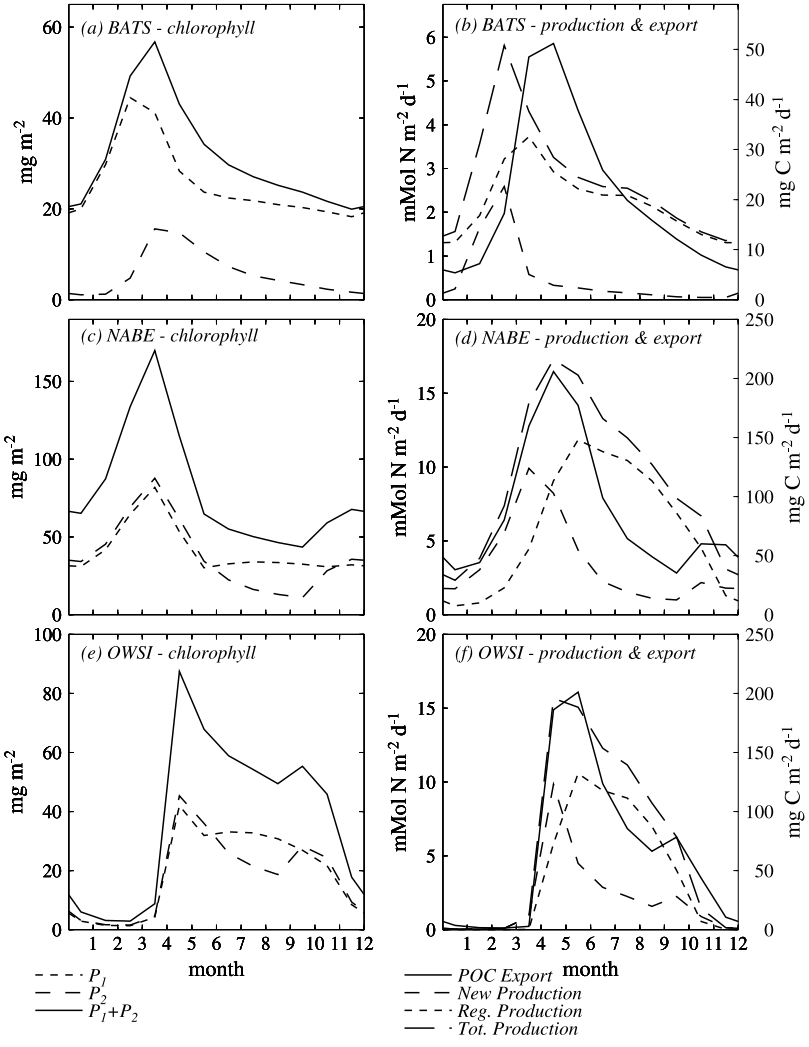

Figure 10. Time series of monthly climatological means of vertically integrated chlorophyll concentration (mg m^{-2}), from the picophytoplankton (P_1), diatoms (P_2), and all phytoplankton (P_1 + P_2), vertically integrated new and regenerated production (mMol N m^{-2} d^{-1}) and export of particulate organic carbon (mg C m^{-2} d^{-1}) at 107 m from the model at the locations corresponding to the (a and b) BATS, (c and d) NABE, and (e and f) OWSI sites.

site. The spatial pattern of silica limitation is consistent with those from global ecosystem models with multinutrient limitation [*Moore et al.*, 2002a, 2004; *Aumont et al.*, 2003]. For the reference case, diatoms are a relatively small component of the phytoplankton community (Figure 2c). Primary production is mostly regenerated, associated with the picophytoplankton (Figure 2f), and diatoms are responsible for a disproportionately large amount of the new/export production (Figure 2e).

[36] In a sensitivity experiment where silica limitation is turned off (Table 3), diatoms consume more nitrogenous nutrients driving down NO_3^- and NH_4^+ concentrations in the euphotic zone, diatom relative abundance and total phytoplankton biomass increase, and the contribution of diatoms to new, regenerated and therefore total production increases. However, the intensification of the vertical particle flux associated the the higher diatom abundance reduces the residence time of sinking detritus and results in a significant drop in NH_4^+ concentrations and regenerated production in the euphotic zone, which depends mostly on the picophytoplankton. The combined increase in new and regenerated production by the diatoms is not large enough to offset the reduction in production by the picophytoplankton, resulting in a decrease in total primary production in the euphotic zone (Table 3). These results are consistent with those from a similar sensitivity experiment by *Aumont et al.* [2003], in which silica limitation for the diatoms is relaxed in a global ecosystem model.

[37] In all three JGOFS sites, the absence of silica limitation results in a increase in the diatom's relative abundance and a decline in picophytoplankton biomass (Figures 13a, 13c, and 13e). At BATS, where the picophytoplankton is the dominant group, total phytoplankton

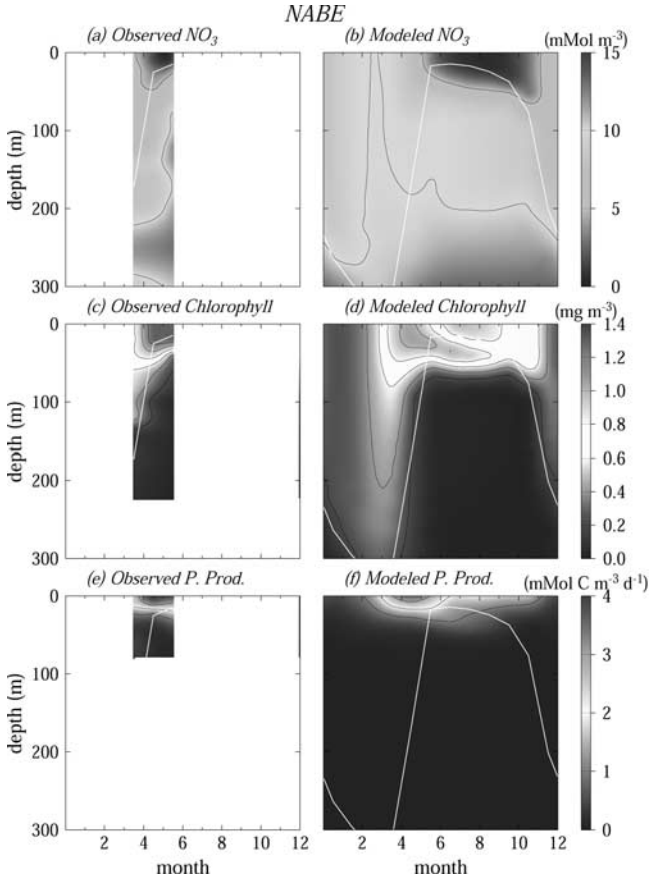

Figure 11. Time series of monthly climatological means of observed and modeled (a and b) NO_3^- (mMol m^{-3}), (c and d) chlorophyll concentrations (mg Chl m^{-3}), and (e and f) primary production (mMol C m^{-3} d^{-1}) at the NABE site. White line represents mixed layer depth. See color version of this figure at back of this issue.

biomass decreases. At BATS and NABE, the higher export flux associated with the higher diatom abundance causes a reduction in regenerated (and total) production (Figures 13b and 13d). At OWSI, however, diatoms are more abundant during the summer than at NABE (Figure 8) and the increase in regenerated production by the diatoms compensates for the drop in regenerated production by the picophytoplankton, resulting in a small increase in total primary production (Figure 13f). At BATS, the effect of lack of silica limitation is smallest during the spring bloom season, when diatoms are mostly nitrogen limited (Figures 13a and 13b).

[38] Model skill for chlorophyll is adversely affected by the removal of silica limitation, particularly the monthly-time case (Figure 5a). In the absence of silica limitation, the decrease in regenerated production caused by the intensification of the particle flux causes a drop in picophytoplankton and total phytoplankton chlorophyll along the upwelling regions off the coast of Africa and inside the oligotrophic gyre (not shown). This effect is most pronounced in the summer. In addition, diatom and total chlorophyll concentrations in temperate and subpolar regions are further overestimated during spring and early summer. These effects increase the amplitude of variation of the model's chlorophyll fields with respect to the satellite's and reduce the correlation between simulated and satellite fields (Figure 5a). The removal of silica limitation has a similar but less noticeable effect on model skill for primary productivity (Figure 5c).

[39] In our model, the effects of silica limitation and species/size structure in the model are directly linked, as silica limitation controls over much of the domain the spatial and temporal shifts between a picophytoplankton-suspended detritus and a diatom-sinking detritus dominated community. In the absence of silica limitation, model behavior is similar to that of a simple NPZD model with one phytoplankton species and one large sinking detritus compartment. The similarity between the error patterns under the no silica limitation sensitivity simulation and previous model studies suggests that an intermediate level

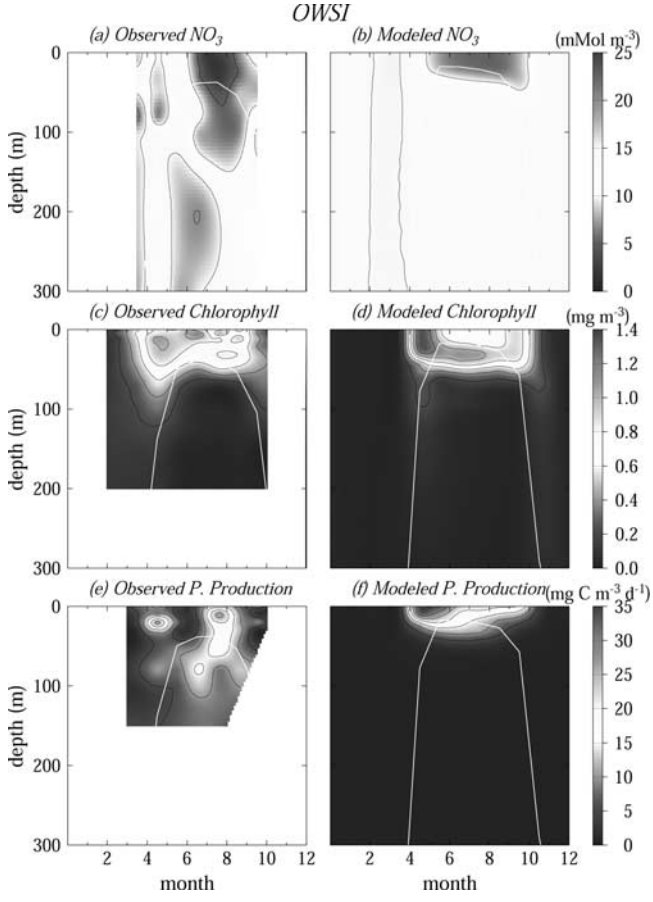

Figure 12. Time series of monthly climatological means of observed and modeled (a and b) NO_3^- (mMol m^{-3}), (c and d) chlorophyll concentrations (mg Chl m^{-3}), and (e and f) primary production (mg C m^{-3} d^{-1}) at the OWSI site. White line represents mixed layer depth. See color version of this figure at back of this issue.

Table 3. Euphotic Zone Averages for the Last 3 Years of the Main Run and the "No Silica Limitation" (NSLIM) Run and the Percentage Difference Between the Two Runs (NSLIM - Main)

	Main Run	NSLIM Run	Percent Difference
Nutrients, mMol N m^{-3}			
NO_3^-	4.0164	3.5891	−10.64
NH_4^+	0.0537	0.0291	−45.81
Phytoplankton biomass, mMol C m^{-3}			
Picophytoplankton	1.1489	1.1672	1.59
Diatoms	0.2762	0.4640	67.99
Total	1.4251	1.6312	14.46
Primary production, mMol C m^{-3} d^{-1}			
Picophytoplankton	0.2892	0.2098	−27.46
Diatoms	0.0563	0.0979	73.89
Total	0.3454	0.3077	−10.91
New production, mMol N m^{-3} d^{-1}			
Picophytoplankton	0.0043	0.0033	−23.26
Diatoms	0.0051	0.0065	27.45
Total	0.0094	0.0097	3.19
Regenerated production, mMol N m^{-3} d^{-1}			
Picophytoplankton	0.0349	0.0191	−45.27
Diatoms	0.0045	0.0072	60.00
Total	0.0393	0.0263	−33.08
Vertical particle flux, mMol C m^{-2} d^{-1}	3.5751	4.8287	35.06

of complexity is required to capture the observed basin-scale variability.

7. Role of Horizontal Advection in the Subtropics

[40] In the model, horizontal advection is an important source of inorganic nutrients and dissolved organic matter for the plankton community in the subtropical gyre (Figure 14). Except for the Gulf Stream region and the eastern boundary, where transport is northward, the meridional advective transport is mostly southward, from higher latitudes into the central region of the subtropical gyre. Years with strong southward transport of nutrients (NO_3^- and SiO_3) and chlorophyll correspond to larger spring blooms and an increase in diatom relative abundance at BATS (Figure 14f). Diatoms are normally a comparatively small component of the phytoplankton community at BATS but with significant interannual variability in their relative abundance and strong episodic blooms [*Hulburt*, 1990; *Siegel et al.*, 1990; *Michaels and Knap*, 1996; *Steinberg et al.*, 2001]. Diatoms blooms at BATS occur in late spring and early summer, indicating that they are not directly related to the increased nutrient input during winter mixing. *Steinberg et al.* [2001] attributes the diatom blooms to local nutrient input/injection by episodic events, such as mesoscale eddies. The model results suggest that the occurrence and strength of diatom blooms at BATS could be related to interannual variations in the advective/meridional transport of nutrients (mainly SiO_3) and cells from higher latitudes. The severe silica limitation for diatoms after the spring bloom at BATS (Figure 9) is consistent with this hypothesis.

[41] The lateral advection of *DON* from areas of higher biological production in the north (Figure 14c) is another important source of nitrogen for the phytoplankton (mostly picophytoplankton) in the oligotrophic gyre, where primary production is based on intense recycling of nutrients (Figures 8a and 10b). Sensitivity experiments using only one single large sinking detritus compartment produced significantly lower primary production rates and chlorophyll concentrations over a considerably larger area of the subtropical gyre (not shown). The importance of the suspended detritus → ammonium → picophytoplankton pathway for maintaining background chlorophyll concentrations is evident when we compare the relative magnitude of the annual mean distributions of detritus remineralization and new and regenerated production by the picophytoplankton and diatoms (Figure 15). Our results are consistent with the climatological analysis of *Williams and Follows* [1998], which demonstrates that southward surface Ekman flow transfers significant amounts of inorganic and organic nutrients from the subpolar into the subtropical gyre.

8. Discussion

[42] It is evidently difficult to model an entire ocean basin with its wide range of biogeographical provinces and diverse plankton communities with one single set of parameters. However, our multinutrient, multispecies formulation seems to provide enough flexibility to begin to represent biological processes in both tropical/subtropical and high latitude areas of the North Atlantic. The model also reproduces observed characteristics of the ecosystem dynamics, e.g., the dominance of the picophytoplankton and episodic diatom blooms in the subtropics, the nutrient-controlled seasonal succession in the phytoplankton community at higher latitudes, and the associated seasonal/depth changes in new and regenerated production and export of particulate carbon.

[43] While not a full measure of model performance, we introduce formal, quantitative metrics of model skill using the Taylor diagram approach (time-space variance, model pattern correlation, and RMS error) with satellite ocean color and primary productivity estimates. The main discrepancy between model open ocean results and observations is the overestimation of chlorophyll concentrations and primary production along the northern edge of the subtropical gyre, due to excessive convective mixing in winter from the physical model. This systematic error is

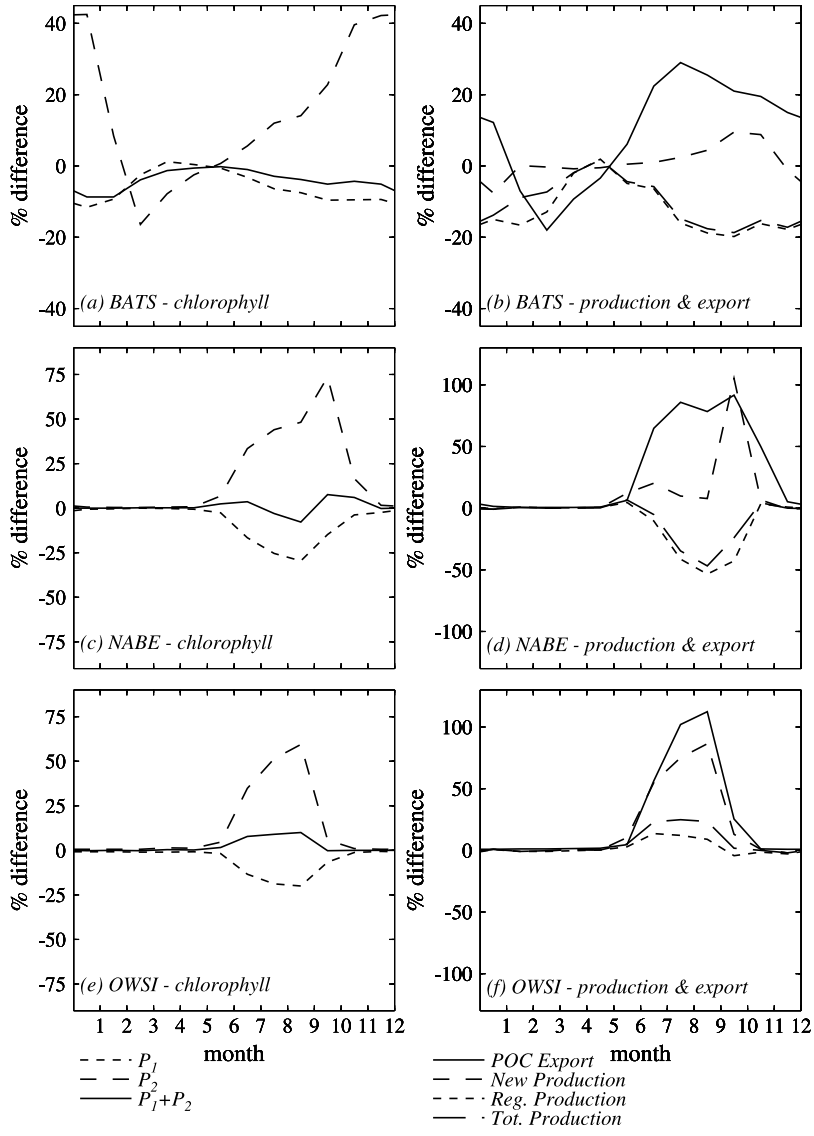

Figure 13. Time series of the percentage difference in monthly climatological means of vertically integrated chlorophyll concentration (mg m^{-2}), from the picophytoplankton (P_1), diatoms (P_2) and all phytoplankton ($P_1 + P_2$), vertically integrated new and regenerated production (mMol N m^{-2} d^{-1}), and export of particulate organic carbon (mg C m^{-2} d^{-1}) at 107 m between the "no silica limitation" run and the main run at the locations corresponding to the (a and b) BATS, (c and d) NABE, and (e and f) OWSI sites.

remarkably insensitive to changes in the OGCM's vertical mixing parameterization, indicating probable deficiencies in the surface forcing fields. The fact that *Oschlies and Garçon* [1999] and *Oschlies et al.* [2000] report similar errors in their eddy-permitting simulations suggests that the problem is not related to our model's lower resolution. We are currently investigating ways to eliminate or minimize or this problem. Another significant difference between model and observations is the underestimation of chlorophyll concentrations and primary production along the coastal areas. This is a result of the model's spatial resolution, which does not capture coastal processes very well.

[44] Our model shows better skill than many previous attempts in simulating the general spatial and temporal patterns in nutrients, chlorophyll and primary production seen in in situ and satellite data. A persistent feature in earlier ecosystem models, including both coarse-resolution [*Sarmiento et al.*, 1993; *Fasham et al.*, 1993] and eddy-permitting [*Oschlies and Garçon*, 1998; *Oschlies et al.*, 2000; *Oschlies*, 2001, 2002] simulations, is the severe underestimation of chlorophyll concentrations and primary production rates in the oligotrophic subtropical gyre. The coarse-resolution (3.5°) global ecosystem model of *Aumont et al.* [2003] also significantly underestimates chlorophyll concentrations over large portions of the subtropical gyre in

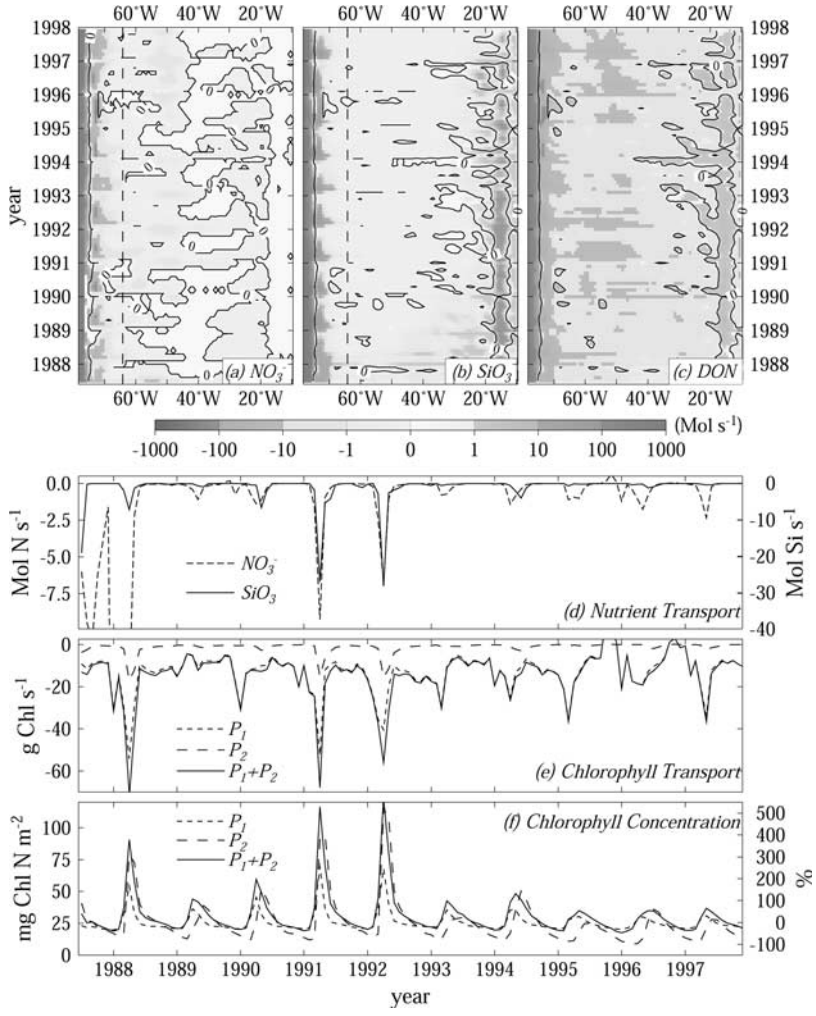

Figure 14. Time series of the meridional transport (Mol s^{-1}) of (a) NO_3^-, (b) SiO_3, and (c) dissolved organic carbon (DON) in the top 107 m across 31°32′N (around the BATS site). The dashed lines in Figures 14a and 14b correspond to the longitude of the BATS site and (d) the nutrient transport time series plot. (e) Time series of the meridional transport of picophytoplankton and diatom chlorophyll at the same location. Positive and negative values indicate northward and southward transport, respectively. (f) Time series of monthly means of total vertically integrated chlorophyll ($P_1 + P_2$) concentrations (mg m^{-2}) and the percentage change in picophytoplankton (P_1) and diatom (P_2) chlorophyll concentrations in relation to their respective means. See color version of this figure at back of this issue.

the North Atlantic. In the present study, chlorophyll and primary production values in the subtropical gyre, while still lower than satellite estimates, are considerably higher and more realistic. Chlorophyll concentrations below 0.02 mg m^{-3} occur only over a relatively small area in the center of the gyre, and minimum chlorophyll and primary production values in the summer are only 50% lower that satellite derived measurements. Lower than observed chlorophyll and primary production values in the subtropical gyre are expected, as the model does not include episodic upwelling of nutrients by mesoscale eddies [*McGillicuddy et al.*, 1998; *Siegel et al.*, 1999; *Garçon et al.*, 2001; *McGillicuddy et al.*, 2003] and the fixation of atmospheric nitrogen (N_2) by cyanobacteria [*Michaels and Knap*, 1996; *Gruber and Sarmiento*, 1997; *Capone et al.*, 1997; *Lipschultz et al.*, 2002].

[45] The simulations of the seasonal cycle of nutrients, chlorophyll and primary production at the JGOFS sites presented here also show significant improvements with respect to those from previous similar studies [*Fasham et al.*, 1993; *Oschlies et al.*, 2000]. Despite the overestimation in winter mixing, maximum nitrate and chlorophyll concentrations in winter and early spring at the actual BATS site are significantly lower and more realistic in the present model (0.12 mMol N m^{-3} and 0.5 mg Chl m^{-3} compared to 1.4 mMol N m^{-3} and 1.2 mg Chl m^{-3} of *Oschlies et al.* [2000], and 3.5 mMol N m^{-3} and 5.5 mg Chl m^{-3} of *Fasham et al.* [1993]). Primary production levels during the summer at BATS are also considerably higher and closer to observations than those reported by *Fasham et al.* [1993] and *Oschlies et al.* [2000]. Simulated annual new production at the BATS

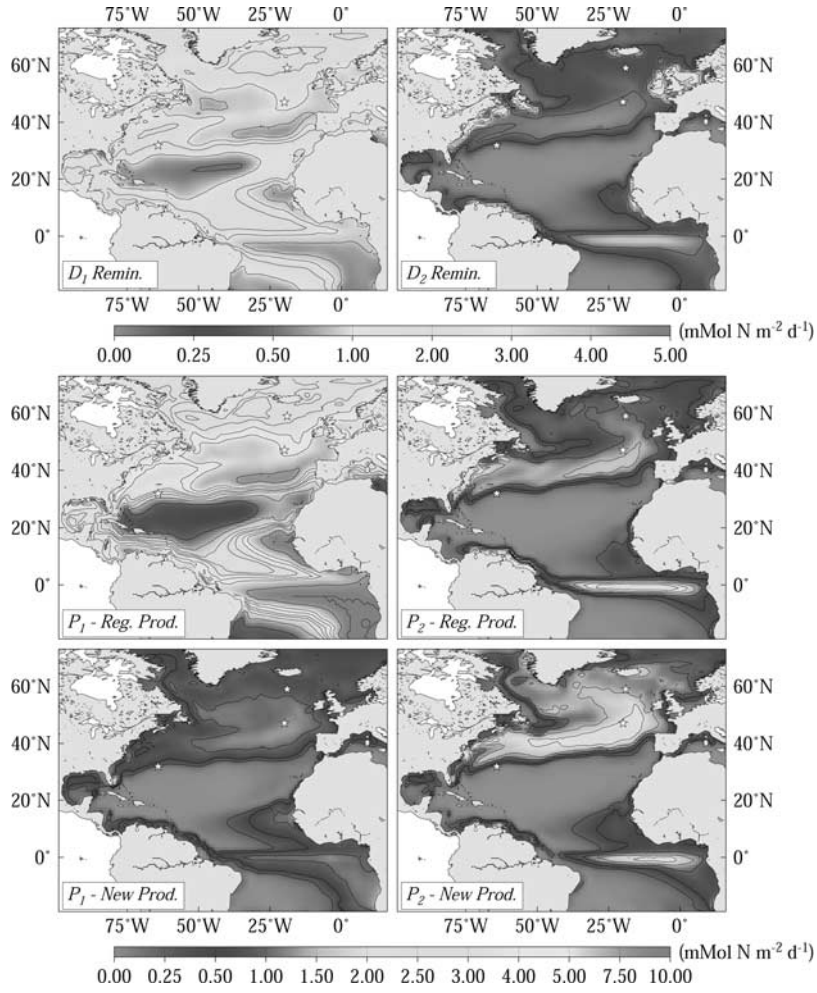

Figure 15. Annual mean distribution of vertically integrated suspended (D_1) and sinking (D_2) detritus remineralization (mMol N m^{-2} d^{-1}) and new and regenerated production by the picophytoplankton (P_1) and diatoms (P_2) (mMol N m^{-2} d^{-1}). See color version of this figure at back of this issue.

location (0.21 Mol N m^{-2} yr^{-1}) is lower than most observational estimates [see *McGillicuddy et al.*, 2003, Table 5] which is to be expected as noted above. At NABE, *Oschlies et al.* [2000] overestimates phytoplankton biomass during the spring bloom by 30%, and their single-phytoplankton, single-detritus model fails to capture the positive correlation between phytoplankton biomass and particle export during and after the spring bloom. In addition, the termination of the bloom is dependent on an unrealistically large peak in zooplankton. In the present study, phytoplankton biomass during the spring bloom is 40% lower than in situ measurements but agrees well with satellite estimates, and the observed nutrient-controlled changes in phytoplankton abundance and vertical particle flux are nicely reproduced by the model. At OWSI, *Fasham et al.* [1993] overestimates chlorophyll concentrations and primary production rates during the spring bloom by more than 200%. In contrast, our model reproduces the magnitude and amplitude of variation of primary production rates at OWSI correctly, and fits the observed seasonal cycle of chlorophyll data remarkably well. Model estimates of annual new production at NABE (1.25 Mol N m^{-2} yr^{-1}) and OWSI (0.80 Mol N m^{-2} yr^{-1}) are also within the range of observed values [see *McGillicuddy et al.*, 2003, Table 5].

[46] The fact that the eddy-permitting experiments of *Oschlies et al.* [2000], which include important nutrient inputs by mesoscale variability, provide only a relatively modest improvement over the results from the coarse-resolution models of *Sarmiento et al.* [1993] and *Fasham et al.* [1993] in the subtropical gyre suggests that a more realistic representation of the physical environment alone is not sufficient to simulate the observed biological fields and processes and that ecosystem dynamics are an important factor controlling biological production. The results presented here support this hypothesis. In the present study, the explicit inclusion of the suspended detritus → ammonium → picophytoplankton pathway in an intermediate resolution OGCM results in a significant improvement in the simulations in the oligotrophic subtropical gyre. In high-resolution experiments, chlorophyll and primary production levels in the subtropical gyre remain abnormally low

despite the more realistic simulation of nutrient inputs by mesoscale processes, due to considerable underestimation of regenerated production by the simple ecosystem model [e.g., *Oschlies et al.*, 2000; *Oschlies*, 2002]. Conversely, coarse-resolution models with increased ecological complexity (multinutrient limitation and suspended and sinking detritus) [e.g., *Aumont et al.*, 2003] also tend to significantly underestimate chlorophyll concentrations in the subtropical gyre because of inadequate representation of the physical environment.

[47] The sensitivity experiments show that the inclusion of silica limitation for the diatoms results in an improvement in model skill. The sensitivity experiments also highlight the importance of diatoms in the ocean's carbon cycle and indicate that a reduction in silica limitation leads to a overall decrease in total primary production in the euphotic zone, through community shifts and counteracting effects of higher new/export production and lower regenerated production. This has important implications for projecting future climate change scenarios as floristic shifts, induced by climate variability, may have a significant impact on oceanic uptake of anthropogenic CO_2 [*Boyd and Doney*, 2002].

[48] Marine ecosystems are composed of a diverse mixture of taxonomically and biogeochemically distinct groups. However, computational costs and the difficulty in parameterizing complex food webs impose severe limits on the construction of realistic ecosystem models. In fact, determining the required level of complexity to accurately simulate the marine ecosystem's response to climate change is one of the major issues confronting biological oceanographers today [*Doney*, 1999; *Denman*, 2003]. The present study suggests that an intermediate level of complexity above simple NPZD models is required for capturing basin-scale patterns of phytoplankton abundance and primary production, particularly in the oligotrophic gyre. We are currently working on expanding the ecosystem model to include additional phytoplankton functional groups (diazotrophs and coccolithophores) and limiting nutrients (phosphate and iron) and improving our physical forcing (e.g., including the diurnal cycle in light intensity) to address global-scale issues [*Moore et al.*, 2004].

Appendix A: Taylor Diagram

[49] A Taylor diagram provides a measure of the degree of pattern correspondence between a "reference" field, usually representing observations, and a "test" or model simulated field [*Taylor*, 2001]. This diagram combines the correlation coefficient (R) and the RMS difference (E) between the two fields along with the ratio of the standard deviations of the two patterns ($\sigma_{test}/\sigma_{ref}$) into one point in a two-dimensional plot (Figure 5). The ratio of the standard deviations indicates the relative amplitude of the simulated and observed variations, while the correlation coefficient indicates whether the fields have similar patterns of variation, regardless of amplitude. The normalized RMS difference reflects differences in the overall pattern of variations. In the diagram, the radial distances from the origin are proportional to the ratio of the standard deviations and the azimuthal positions give the correlation between the two fields (Figure 5). The point representing the reference field is plotted along the abscissa and has coordinate $\sigma_{ref}/\sigma_{ref} = 1$ and $R = 1$. The distance between the test and reference point is proportional to the normalized RMS difference between the two fields.

[50] Consider a test field p and a reference field q defined in a $M \times N$ spatial grid and in T points in time, where each time (t) represents a monthly mean ($t = \{1, 2,\ldots,12\}$). The area of each grid cell is given by $a_{i,j}$ ($i = \{1, 2,\ldots,M\}$; $j = \{1, 2, \ldots,N\}$).

A1. Total Time-Space Case

[51] In the total time-space case the standard deviations for p and q are computed as:

$$\sigma_p = \sqrt{\frac{\sum_j^N \sum_i^M \left[a_{i,j} \sum_t^T \left(p_{i,j,t} - p_{\overline{i,j,t}} \right)^2 \right]}{T \sum_j^N \sum_i^M a_{i,j}}};$$

$$\sigma_q = \sqrt{\frac{\sum_j^N \sum_i^M \left[a_{i,j} \sum_t^T \left(q_{i,j,t} - q_{\overline{i,j,t}} \right)^2 \right]}{T \sum_j^N \sum_i^M a_{i,j}}}$$

where $p_{\overline{i,j,t}}$ and $q_{\overline{i,j,t}}$ are total time-space means.The correlation coefficient between p and q is given by:

$$R = \frac{\sum_j^N \sum_i^M \left[a_{i,j} \sum_t^T \left(p_{i,j,t} - p_{\overline{i,j,t}} \right) \left(q_{i,j,t} - q_{\overline{i,j,t}} \right) \right]}{\sigma_p \sigma_q T \sum_j^N \sum_i^M a_{i,j}}$$

And the RMS difference is calculated as:

$$E = \sqrt{\frac{\sum_j^N \sum_i^M \left\{ a_{i,j} \sum_t^T \left[\left(p_{i,j,t} - p_{\overline{i,j,t}} \right) - \left(q_{i,j,t} - q_{\overline{i,j,t}} \right) \right]^2 \right\}}{T \sum_j^N \sum_i^M a_{i,j}}}$$

A2. Monthly-Time Case

[52] In the monthly-time case the standard deviations, correlation coefficients and RMS difference for each field are computed in the same way as in the total time-space case, except that deviations are computed with respect to the temporal (annual) means at each grid point $p_{i,j,\bar{t}}$ and $q_{i,j,\bar{t}}$.

A3. Spatial-Annual Case

[53] In the spatial-annual case the standard deviation for fields p and q are computed as

$$\sigma_p = \sqrt{\frac{\sum_j^N \sum_i^M a_{i,j}\left(p_{i,j,\bar{t}} - p_{\overline{i,j,t}}\right)^2}{\sum_j^N \sum_i^M a_{i,j}}};$$

$$\sigma_q = \sqrt{\frac{\sum_j^N \sum_i^M a_{i,j}\left(q_{i,j,\bar{t}} - q_{\overline{i,j,t}}\right)^2}{\sum_j^N \sum_i^M a_{i,j}}}$$

The correlation coefficient between p and q is calculated as:

$$R = \frac{\sum_j^N \sum_i^M a_{i,j}\left(p_{i,j,\bar{t}} - p_{\overline{i,j,t}}\right)\left(q_{i,j,\bar{t}} - q_{\overline{i,j,t}}\right)}{\sigma_p \sigma_q \sum_j^N \sum_i^M a_{i,j}}$$

And the RMS difference is given by:

$$E = \sqrt{\frac{\sum_j^N \sum_i^M a_{i,j}\left[\left(p_{i,j,\bar{t}} - p_{\overline{i,j,t}}\right) - \left(q_{i,j,\bar{t}} - q_{\overline{i,j,t}}\right)\right]^2}{\sum_j^N \sum_i^M a_{i,j}}}$$

A4. Monthly-Spatial Case

[54] In the monthly-spatial case the standard deviations, correlation coefficients and RMS difference for p and q at each month (t) are computed in the same way as in the spatial-annual case, except that the deviations are given by $p_{i,j,t} - p_{\overline{i,j,t}}$ and $q_{i,j,t} - q_{\overline{i,j,t}}$, where $p_{\overline{i,j,t}}$ and $q_{\overline{i,j,t}}$ are spatial means for each month (t).

[55] **Acknowledgments.** We thank Joanie Kleypas, Keith Lindsay and Keith Moore for their help in the development of the ecosystem model and for stimulating discussions pertaining to this work. Support for this work was provided by NASA SeaWiFS grant W-19,223 and NSF JGOFS SMP grant 0222033. The authors gratefully acknowledge the NCAR Climate Simulation Laboratory for the computer time provided. This is WHOI contribution 11204 and U.S. JGOFS contribution 1050.

References

Armstrong, R. A. (1999), Stable model structures for representing biogeochemical diversity and size spectra in plankton communities, *J. Plankton Res.*, *21*(3), 445–464.

Aumont, O., E. Maier-Reimer, S. Blain, and P. Monfray (2003), An ecosystem model of the global ocean including Fe, Si, P colimitations, *Global Biogeochemical Cycles*, *17*(2), 1060, doi:10.1029/2001GB001745.

Barnier, B., L. Siefridt, and P. Marchesiello (1995), Thermal forcing for a global ocean circulation model using a three-year climatology of ECMWF analyses, *J. Mar. Syst.*, *92*, 11,709–11,726.

Behrenfeld, M., and P. Falkowski (1997), Photosynthetic rates derived from satellite-based chlorophyll concentration, *Limnol. Oceanogr.*, *42*(1), 1–20.

Bidigare, R. R. (1983), Nitrogen excretion by marine zooplankton, in *Nitrogen in the Marine Environment*, edited by E. J. Carpenter and D. G. Capone, pp. 385–409, Academic, San Diego, Calif.

Boyd, P. W., and S. C. Doney (2002), Modeling regional responses by marine pelagic ecosystems to global climate change, *Geophys. Res. Lett.*, *29*(16), 1806, doi:10.1029/2001GL014130.

Brzezinski, M. A. (1985), The Si:C:N ratio of marine diatoms: Interspecific variability and the effect of some environmental variables, *J. Phycol.*, *21*, 347–359.

Brzezinski, M. A., and D. M. Nelson (1989), Seasonal changes in the silicon cycle within a Gulf Stream warm-core ring, *Deep Sea Res.*, *Part I*, *36*, 1009–1030.

Brzezinski, M. A., and D. M. Nelson (1995), The annual silica cycle in the Sargasso Sea near Bermuda, *Deep Sea Res.*, *Part I*, *42*, 1215–1237.

Brzezinski, M. A., and D. M. Nelson (1996), Chronic substrate limitation of silicic acid uptake rates in the western Sargasso Sea, *Deep Sea Res.*, *Part II*, *43*, 437–453.

Buesseler, K. O., M. P. Bacon, J. K. Cochran, and H. D. Livington (1992), Carbon and nitrogen export during the JGOFS North Atlantic Bloom Experiment estimated from ^{234}Th:^{238}U disequilibria, *Deep Sea Res.*, *Part A*, *39*, 1115–1137.

Campbell, J. W. (1995), The lognormal distribution as a model for bio-optical variability in the sea, *J. Geophys. Res.*, *100*, 13,237–13,254.

Campbell, J. W., et al. (2002), Comparison of algorithms for estimating ocean primary production from surface chlorophyll, temperature and irradiance, *Global Biogeochem. Cycles*, *16*(3), 1035, doi:10.1029/2001GB001444.

Capone, D. G., J. P. Zehr, H. W. Paerl, B. Bergman, and E. J. Carpenter (1997), *Trichodesmium*, a globally significant marine cyanobacterium, *Science*, *276*, 1221–1229.

Christian, J. R., M. A. Verschell, R. Murtugudde, A. J. Busalacchi, and C. R. McClain (2002a), Biogeochemical modeling of the tropical Pacific Ocean I: Seasonal and interannual variability, *Deep Sea Res.*, *Part II*, *49*, 509–543.

Christian, J. R., M. A. Verschell, R. Murtugudde, A. J. Busalacchi, and C. R. McClain (2002b), Biogeochemical modeling of the tropical Pacific Ocean II: Iron biogeochemistry, *Deep Sea Res., Part II*, *49*, 545–565.

Conkright, M., S. Levitus, and T. Boyer (1994), *World Ocean Atlas 1994*, vol. 1, *Nutrients*, *NOAA Atlas NESDIS 1*, U.S. Gov. Print. Off., Washington, D. C.

Denman, K. L. (2003), Modelling planktonic ecosystems: Parameterizing complexity, *Prog. Oceanogr.*, *57*, 429–452.

Denman, K. L., and M. A. Peña (1999), A coupled 1-D biological/physical model of the northeast subartic Pacific Ocean with iron limitation, *Deep Sea Res.*, *Part II*, *46*, 2877–2908.

Doney, S. C. (1999), Major challenges confronting marine biogeochemical modeling, *Global Biogeochem. Cycles*, *13*(3), 705–714.

Doney, S. C., D. M. Glover, and R. G. Najjar (1996), A new coupled, one-dimensional biological-physical model for the upper ocean: Applications to the JGOFS Bermuda Atlantic Time-series Study (BATS) site, *Deep Sea Res.*, *Part II*, *43*, 591–629.

Doveri, F., M. Scheffer, S. Rinaldi, S. Muratori, and Y. Kuznetsov (1993), Seasonality and chaos in a plankton-fish model, *Theoretical Popul. Biol.*, *43*(2), 159–183.

Dukowicz, J. K., and R. D. Smith (1994), Implicit free-surface method for the Bryan-Cox-Semtner ocean model, *J. Geophys. Res.*, *99*, 7991–8014.

DuRand, M. D., R. J. Olson, and S. W. Chisholm (2001), Phytoplankton population dynamics at the Bermuda Atlantic Time-Series station in the Sargasso Sea, *Deep Sea Res.*, *Part II*, *48*, 1983–2003.

Dutkiewicz, S., M. Follows, J. Marshall, and W. W. Gregg (2001), Interannual variability of phytoplankton abundances in the North Atlantic, *Deep Sea Res.*, *Part II*, *48*, 2323–2344.

Eppley, R. W., and B. J. Peterson (1979), Particulate organic matter flux and planktonic new production in the deep ocean, *Nature*, *282*, 677–679.

Fasham, M. J. R., H. W. Ducklow, and S. M. McKelvie (1990), A nitrogen-based model of plankton dynamics in the oceanic mixed layer, *J. Mar. Res.*, *48*(3), 591–639.

Fasham, M. J. R., J. L. Sarmiento, R. D. Slater, H. W. Ducklow, and R. Williams (1993), Ecosystem behavior at Bermuda Station S and Ocean Weather Station "India": A general circulation model and observational analysis, *Global Biogeochem. Cycles*, *7*, 379–415.

Franks, P. J. S., J. S. Wroblewski, and G. R. Flierl (1986), Behavior of a simple plankton model with food-level acclimation by herbivores, *Mar. Biol.*, *91*(1), 121–129.

Fung, I. Y., S. K. Meyn, S. C. Doney, J. G. John, and J. K. B. Bishop (2000), Iron supply and demand in the upper ocean, *Global Biogeochem. Cycles*, *14*, 281–291.

Garçon, V., A. Oschlies, S. Doney, D. McGillicuddy, and J. Waniek (2001), The role of mesoscale variability on plankton dynamics, *Deep Sea Res., Part II*, *48*, 2199–2226.

Garside, C., and J. C. Garside (1993), The *f*–ratio on 20°W during the North Atlantic Bloom Experiment, *Deep Sea Res., Part II*, *40*, 75–90.

Geider, R. J., H. L. MacIntyre, and T. M. Kana (1997), Dynamic model of phytoplankton growth and acclimation: responses of the balanced growth rate and the chlorophyll *a*:carbon ratio to light, nutrient limitation and temperature, *Mar. Ecol. Prog. Ser.*, *148*, 187–200.

Geider, R. J., H. L. MacIntyre, and T. M. Kana (1998), A dynamic regulatory model of phytoplankton acclimation to light, nutrients, and temperature, *Limnol. Oceanogr.*, *43*(4), 679–694.

Gent, P. R., and J. C. McWilliams (1990), Isopycnal mixing in ocean circulation models, *J. Phys. Oceanogr.*, *20*, 150–155.

Glover, D. M., and P. G. Brewer (1988), Estimates of wintertime mixed layer nutrient concentrations in the North Atlantic, *Deep Sea Res.*, *35*, 1525–1546.

Gregg, W. W. (2002), Tracking the SeaWiFS record with a coupled physical/biogeochemical/radiative model of the global oceans, *Deep Sea Res., Part II*, *49*, 81–105.

Gruber, N., and J. L. Sarmiento (1997), Global patterns of marine nitrogen fixation and denitrification, *Global Biogeochem. Cycles*, *11*, 235–266.

Hadziabdic, P., and R. N. Cramer (1999), Plankton reactivity in the marine environment PRIME data set and user's guide [CD-ROM], Br. Oceanogr. Data Cent., Nat. Environ. Res. Counc., Swindon, U. K.

Harrison, W. G. (1980), Nitrogen regeneration and primary production in the sea, in *Primary Productivity in the Sea*, edited by P. G. Falkowski, *Environ. Sci. Res.*, *19*, 433–460.

Harrison, W. G. (1992), Regeneration of nutrients, in *Primary Productivity and Biogeochemical Cycles in the Sea*, edited by P. G. Falkowski and A. D. Woodhead, *Environ. Sci. Res.*, *43*, 385–407.

Hecht, M. W., F. O. Bryan, and W. R. Holland (1998), A consideration of tracer advection schemes in a primitive equation ocean model, *J. Geophys. Res.*, *103*, 3301–3321.

Hood, R. R., N. R. Bates, D. G. Capone, and D. B. Olson (2001), Modeling the effect of nitrogen fixation on carbon and nitrogen fluxes at BATS, *Deep Sea Res., Part II*, *48*, 1609–1648.

Hulburt, E. M. (1990), Description of phytoplankton and nutrient in spring in the western North Atlantic Ocean, *J. Plankton Res.*, *12*(1), 1–28.

Large, W. G., J. C. McWilliams, and S. C. Doney (1994), Oceanic vertical mixing: A review and a model with a nonlocal boundary layer parameterization, *Rev. Geophys.*, *32*(4), 363–403.

Leonard, C. L., C. R. McClain, R. Murtugudde, E. E. Hofmann, and L. W. Harding Jr. (1999), An iron-based ecosystem model for the central equatorial Pacific, *J. Geophys. Res.*, *104*, 1325–1341.

Lessard, E. J., and M. C. Murrell (1998), Distribution, abundance and size composition of heterotrophic dinoflagellates and ciliates in the Sargasso Sea near Bermuda, *Deep Sea Res., Part I*, *43*, 1045–1065.

Levitus, S., and T. Boyer (1994), *World Ocean Atlas 1994*, vol. 4, *Temperature, NOAA Atlas NESDIS 4*, U.S. Gov. Print. Off., Washington, D. C.

Levitus, S., R. Burgett, and T. Boyer (1994), *World Ocean Atlas 1994*, vol. 3, *Salinity, NOAA Atlas NESDIS 3*, U.S. Gov. Print. Off., Washington, D. C.

Lima, I. D., D. B. Olson, and S. C. Doney (2002), Intrinsic dynamics and stability properties of size-structured pelagic ecosystem models, *J. Plankton Res.*, *24*(6), 533–556.

Lipschultz, F., N. R. Bates, C. A. Carlson, and D. Hansel (2002), New production in the Sargasso Sea: History and current status, *Global Biogeochem. Cycles*, *16*(1), 1001, doi:10.1029/2000GB001319.

Lochte, K. L., H. W. Ducklow, M. J. R. Fasham, and C. Stienen (1993), Plankton succession and carbon cycling at 47°N 20°W during the JGOFS North Atlantic Bloom Experiment, *Deep Sea Res., Part II*, *40*, 91–114.

Longhurst, A. R. (1998), *Ecological Geography of the Sea*, Academic, San Diego, Calif.

Loukos, H., B. Frost, D. E. Harrison, and J. W. Murray (1997), An ecosystem model with iron limitation of primary production in the equatorial Pacific at 140°W, *Deep Sea Res., Part II*, *44*, 2221–2249.

Lowry, R. K., P. Machin, and R. N. Cramer (1994), BOFS North Atlantic data set. Oceanographic data collected during the North Atlantic cruises of the NERC Biogeochemical Ocean Flux Study (1989–1991). A UK contribution to JGOFS, CD and user's guide, Br. Oceanogr. Data Cent., Nat. Environ. Res. Counc., Swindon, U. K.

Mahowald, N., K. Kohfeld, M. Hansson, Y. Balkanski, S. P. Harrison, I. C. Prentice, M. Schulz, and H. Rodhe (1999), Dust sources and deposition during the Last Glacial Maximim and current climate: A comparison of model results with paleodata from ice cores and marine sediments, *J. Geophys. Res.*, *104*, 15,895–15,916.

Mann, K. H., and J. R. Lazier (1991), *Dyanmics of Marine Ecosystems: Biological-Physical Interactions in the Oceans*, Blackwell, Malden, Mass.

Martin, J. H., S. E. Fitzwater, R. M. Gordon, C. N. Hunter, and S. J. Tanner (1993), Iron, primary production and carbon-nitrogen flux studies during the JGOFS North Atlantic Bloom Experiment, *Deep Sea Res., Part II*, *40*, 115–134.

McCarthy, J. J., and E. J. Carpenter (1983), Nitrogen cycling in near-surface waters of the open ocean, in *Nitrogen in the Marine Environment*, edited by E. J. Carpenter and D. G. Capone, pp. 487–512, Academic, San Diego, Calif.

McCreary, J. P., K. E. Kohler, R. R. Hood, and D. B. Olson (1996), A four-component ecosystem model of biological activity in the Arabian Sea, *Prog. Oceanogr.*, *37*, 193–240.

McGillicuddy, D. J., A. R. Robinson, D. A. Siegel, H. W. Jannasch, R. Johnson, T. D. Dickey, J. McNeil, A. F. Michaels, and A. H. Knap (1998), Influence of mesoscale eddies on new production in the Sargasso Sea, *Nature*, *394*, 263–266.

McGillicuddy, D. J., Jr., L. A. Anderson, S. C. Doney, and M. E. Maltrud (2003), Eddy-driven sources and sinks of nutrients in the upper ocean: Results from a 0.1° resolution model of the North Atlantic, *Global Biogeochem. Cycles*, *17*(2), 1035, doi:10.1029/2002GB001987.

Michaels, A. F., and A. H. Knap (1996), Overview of the US JGOFS Bermuda Atlantic Time-series Study and Hydrostation S program, *Deep Sea Res., Part II*, *43*, 157–198.

Moore, J. K., S. Doney, D. M. Glover, and I. Y. Fung (2002a), Iron cycling and nutrient limitation patterns in surface waters of the world ocean, *Deep Sea Res., Part II*, *49*, 463–508.

Moore, J. K., S. Doney, J. A. Kleypas, D. M. Glover, and I. Y. Fung (2002b), An intermediate complexity marine ecosystem model for the global domain, *Deep Sea Res., Part II*, *49*, 403–462.

Moore, J. K., S. C. Doney, and K. Lindsay (2004), Upper ocean ecosystem dynamics and iron cycling in a global 3-D model, *Global Biogeochem. Cycles*, doi:10.1029/2004GB002220, in press.

Nelson, D. M., and M. A. Brzezinski (1997), Diatom growth and productivity in an oligotrophic midocean gyre: A 3-yr record from the Sargasso Sea near Bermuda, *Limnol. Oceanogr.*, *42*, 473–486.

Nelson, D. M., and P. Tréguer (1992), Role of silicon as a limiting nutrient to Antarctic diatoms, *Mar. Ecol. Prog. Ser.*, *80*, 255–264.

Nelson, D. M., M. A. Brzezinski, D. E. Sigmon, and V. M. Franck (2001), A seasonal progression of Si limitation in the Pacific sector of the Southern Ocean, *Deep Sea Res., Part II*, *48*, 3973–3995.

O'Neil, R. V., D. L. Angelis, J. J. Pastor, B. J. Jackson, and W. M. Post (1989), Multiple nutrient limitation in ecological models, *Ecol. Modell.*, *46*, 147–163.

Oschlies, A. (2001), Model-derived estimates of new production: New results point toward lower values, *Deep Sea Res., Part II*, *48*, 2173–2197.

Oschlies, A. (2002), Nutrient supply to the surface waters of the North Atlantic: A model study, *J. Geophys. Res.*, *107*(C5), 3046, doi:10.1029/2000JC000275.

Oschlies, A., and V. Garçon (1998), Eddy-induced enhancement of primary production in a model of the North Atlantic Ocean, *Nature*, *394*, 266–269.

Oschlies, A., and V. Garçon (1999), An eddy-permiting coupled physical-biological models of the North Atlantic: 1. Sensitivity to advection numerics and mixed layer, *Global Biogeochem. Cycles*, *13*, 135–160.

Oschlies, A., W. Koeve, and V. Garçon (2000), An eddy-permitting coupled physical-biological model of the North Atlantic: 2. Ecosystem dynamics and comparison with satellite and JGOFS local studies data, *Global Biogeochem. Cycles*, *14*, 499–523.

Pomeroy, L. (1974), The ocean's food web, a changing paradigm, *BioScience*, *24*, 499–504.

Pondaven, P., D. Ruiz-Pino, C. Fravalo, P. Tréguer, and C. Jeandel (2000), Interannual variability of Si and N cycles at the time-series station KERFIX between 1990 and 1995—A 1-D modelling study, *Deep Sea Res., Part I*, *47*, 223–257.

Sarmiento, J. L., R. D. Slater, M. J. R. Fasham, H. W. Ducklow, J. R. Toggweiler, and G. T. Evans (1993), A seasonal three-dimensional ecosystem model of nitrogen cycling in the North Atlantic euphotic zone, *Global Biogeochem. Cycles*, *7*, 417–450.

Siegel, D. A., R. Itturiaga, R. R. Bidigare, R. C. Smith, H. Pak, T. D. Dickey, J. Marra, and K. S. Baker (1990), Meridional variations of the spring-time phytoplankton community in the Sargasso Sea, *J. Mar. Res.*, *48*, 379–412.

Siegel, D., D. J. McGillicuddy, and E. A. Fields (1999), Mesoscale eddies, satellite altimetry, and new production in the Sargasso Sea, *J. Geophys. Res.*, *104*, 13,359–13,379.

Sieracki, M. E., P. G. Verity, and D. K. Stoecker (1993), Plankton community response to sequential silicate and nitrate depletion during 1989 North Atlantic Bloom Experiment, *Deep Sea Res.*, *Part II*, *40*, 213–225.

Smayda, T. J. (1969), Some measurements of the sinking rate of fecal pellets, *Deep Sea Res.*, *14*, 621–625.

Smith, R. D., J. K. Dukowicz, and R. C. Malone (1992), Parallel ocean circulation modeling, *Physica D*, *60*, 38–61.

Smith, R. D., M. E. Maltrud, F. O. Bryan, and M. W. Hecht (2000), Numerical simulation of the North Atlantic Ocean at 1/10°, *J. Phys. Oceanogr.*, *30*(7), 1532–1561.

Steele, J. H., and E. W. Henderson (1992), The role of predation in plankton models, *J. Plankton Res.*, *14*(1), 157–172.

Steinberg, D. K., C. A. Carlson, N. R. Bates, R. J. Johnson, A. F. Michaels, and A. H. Knap (2001), Overview of the US JGOFS Bermuda Atlantic Time-series Study (BATS): A decade-scale look at ocean biology and biogeochemistry, *Deep Sea Res.*, *Part II*, *48*, 1405–1447.

Taylor, K. E. (2001), Summarizing multiple aspects of model performance in a single diagram, *J. Geophys. Res.*, *106*, 7183–7192.

Tegen, I., and I. Y. Fung (1995), Contribution to the atmospheric mineral aerosol load from land surface modification, *J. Geophys. Res.*, *100*, 18,707–18,726.

Weeks, A. R., M. J. R. Fasham, J. Aiken, D. S. Harbour, J. F. Read, and I. Bellan (1993), The spatial and temporal development of the spring bloom during the JGOFS North Atlantic Bloom Experiment 1989, *J. Mar. Biol. Assoc. U. K.*, *73*(2), 253–282.

Williams, R. G., and M. J. Follows (1998), The Ekman transfer of nutrients and maintenance of new production over the North Atlantic, *Deep Sea Res.*, *Part I*, *45*, 461–489.

Williams, R., and G. A. Robinson (1973), Primary production at Ocean Weather Station India (59°00′, 19°00′) in the North Atlantic, *Bull. Mar. Ecol.*, *8*, 115–121.

Wroblewski, J. S. (1989), A model of the spring bloom in the North Atlantic and its impact on ocean optics, *Limnol. Oceanogr.*, *34*, 1563–1571.

S. C. Doney and I. D. Lima, Woods Hole Oceanographic Institution, Department of Marine Chemistry and Geochemistry, MS 25, 360 Woods Hole Road, Woods Hole, MA 02543, USA. (sdoney@whoi.edu; ilima@whoi.edu)

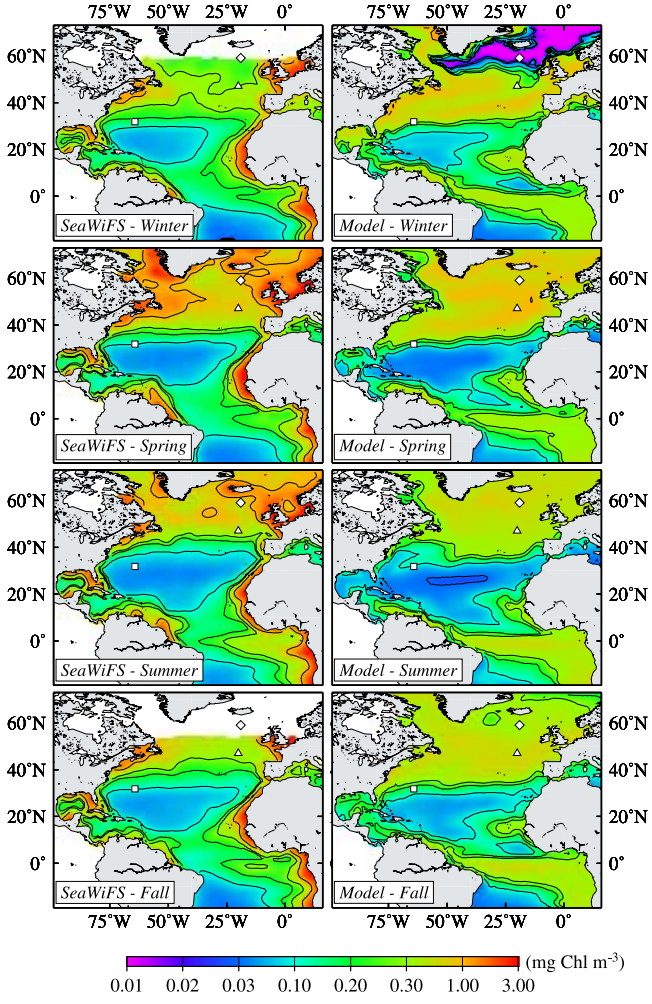

Figure 3. Seasonal climatologies of surface chlorophyll concentrations (mg Chl m^{-3}) from the last 3 years of model integration and SeaWiFS imagery (October 1998 to September 1999). White symbols represent the location of the BATS (squares), NABE (triangles), and OWSI (diamonds) sites.

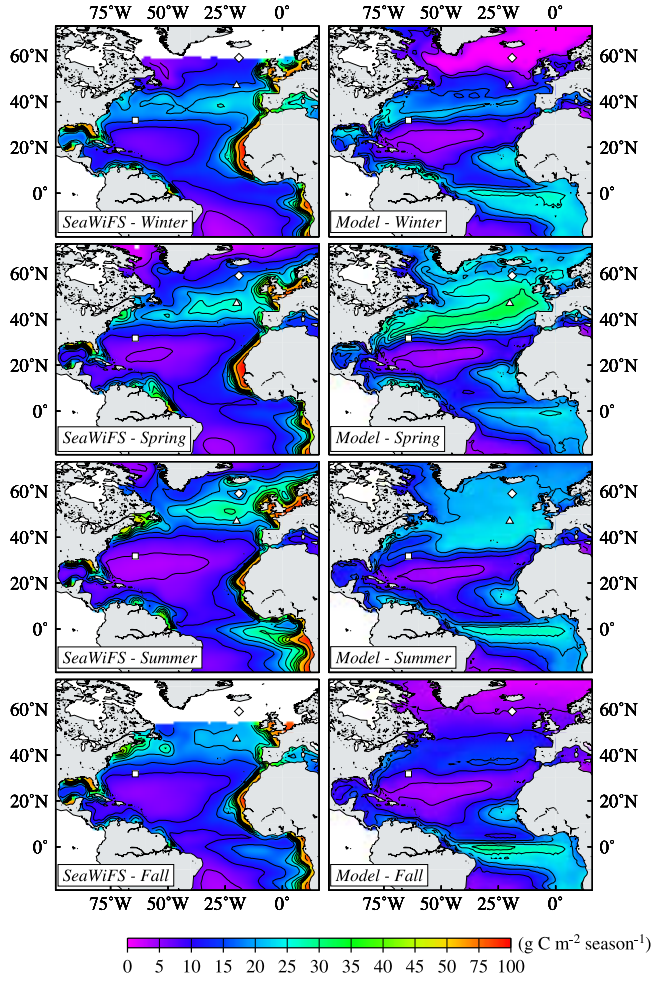

Figure 4. Seasonal climatologies of primary productivity estimates (g C m^{-2} $season^{-1}$) from the last 3 years of model integration and from SeaWiFS chlorophyll data using the VGPM model of *Behrenfeld and Falkowski* [1997]. White symbols represent the location of the BATS (squares), NABE (triangles), and OWSI (diamonds) sites.

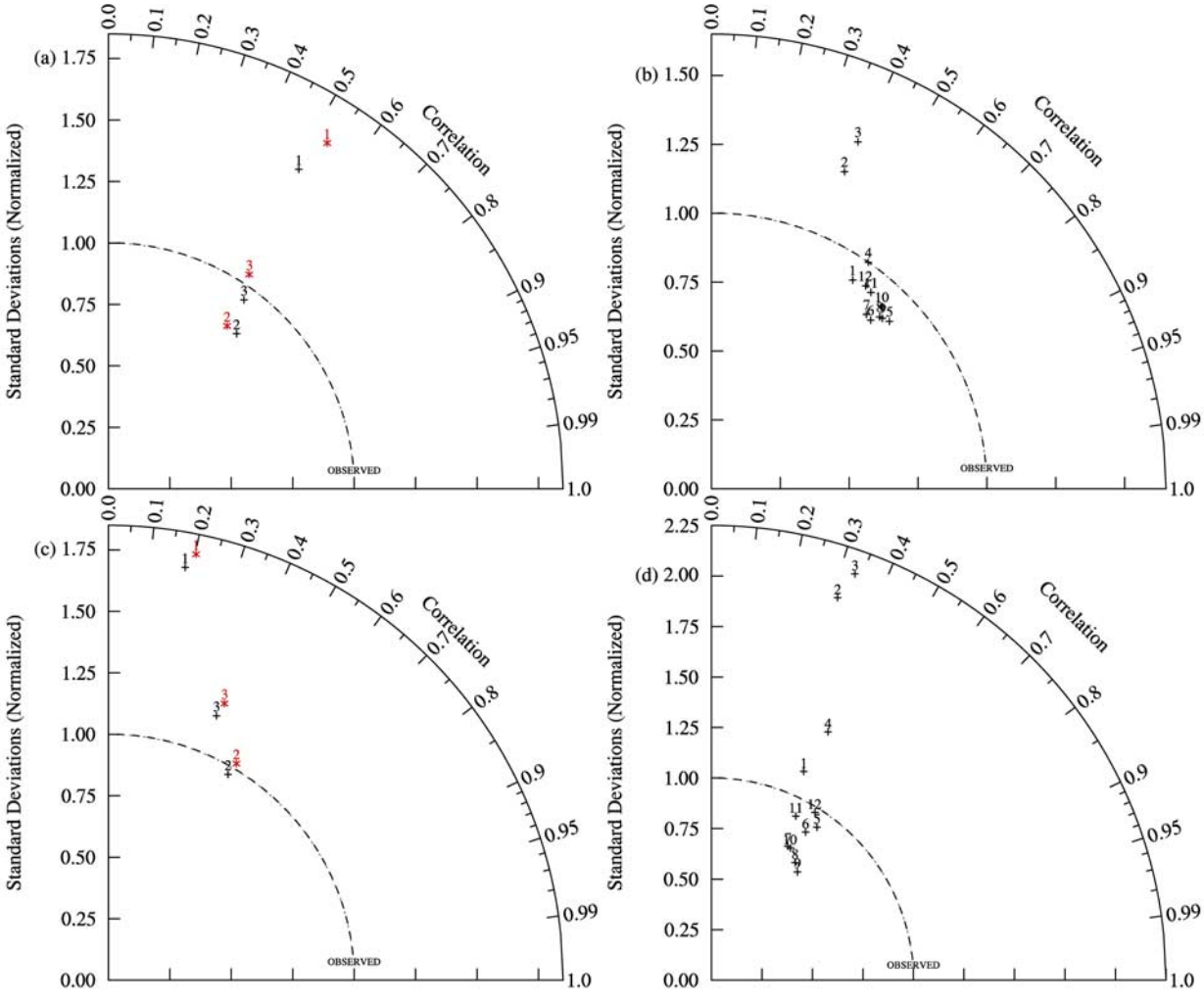

Figure 5. Taylor diagram comparing monthly climatological fields of log transformed surface chlorophyll estimates (mg Chl m^{-3}) from the model and satellite and monthly primary productivity estimates (g C m^{-2} $month^{-1}$) from the model and satellite data using the VGPM model of *Behrenfeld and Falkowski* [1997]. The radial distances from the origin are proportional to the ratio of the model and satellite standard deviations and the azimuthal positions correspond to the correlation between the model and satellite fields. The distances from the model points to the satellite point are proportional to the normalized RMS difference between the fields (Table 2). Black points represent the main run, and red points represent the "no silica limitation" run (NSLIM). (a) Chlorophyll monthly-time (1), spatial-annual (2), and total time-space (3) statistics. (b) Chlorophyll monthly-spatial statistics. (c) Primary productivity monthly-time (1), spatial-annual (2), and total time-space (3). (d) Primary productivity monthly-spatial statistics. Numbers in Figure 5b and 5d correspond to the months of the year.

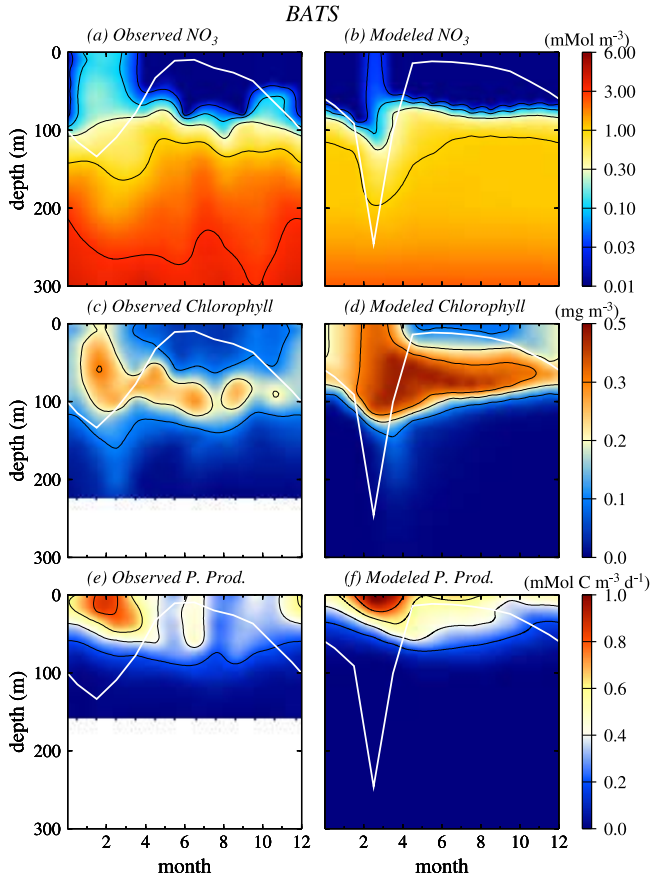

Figure 7. Time series of monthly climatological means of observed and modeled NO_3^- (mMol m^{-3}), chlorophyll concentrations (mg Chl m^{-3}), and primary production (mMol C m^{-3} d^{-1}) at the BATS site. White line represents mixed layer depth.

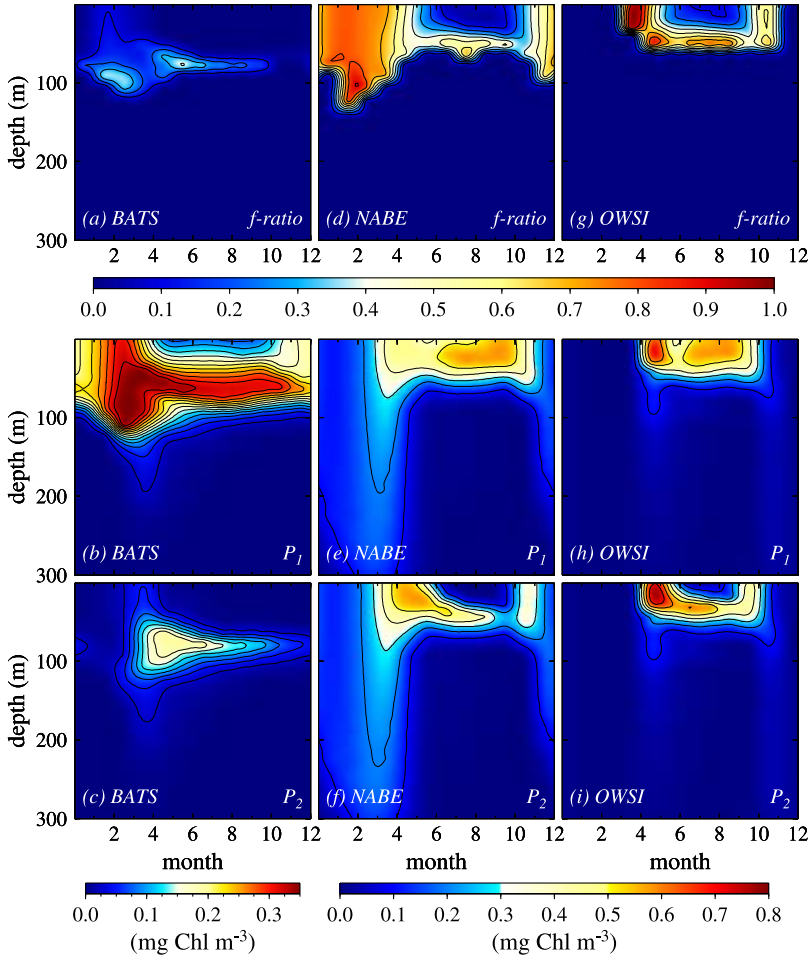

Figure 8. Time series of monthly climatological means of picophytoplankton (P_1) and diatoms (P_2) chlorophyll concentrations (mg m^{-3}) and f ratios as function of depth from the model at the locations corresponding to the (a–c) BATS, (d–f) NABE, and (g–i) OWSI sites. Note different color scale for BATS.

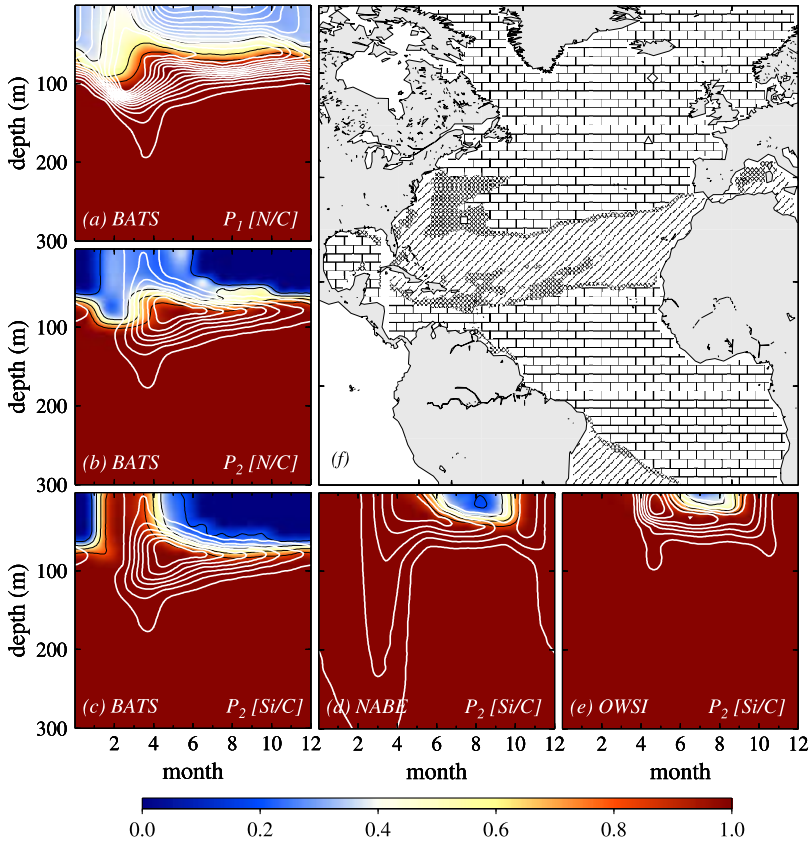

Figure 9. Time series of monthly climatological means of the picophytoplankton (P_1) and diatom (P_2) [N:C] and [Si:C] cell quotas relative to the respective maximum cell quotas as function of depth from the model at the locations corresponding to the (a–c) BATS, (d) NABE, and (e) OWSI sites. [N:C] and [Si:C] values below 0.2 near the surface in Figures 9b and 9c indicate $P_2 = 0$. White contour lines indicate picophytoplankton and diatom chlorophyll concentrations (mg m^{-3}) and correspond to the same contours in Figure 8. (f) Geographical nutrient limitation patterns for the diatoms averaged over the the euphotic zone (107 m). Rectangles indicate silica limitation, inclined lines indicate nitrogen limitation, and the cross-hatch pattern shows where the limiting nutrient varies seasonally. Symbols represent the location of the BATS (square), NABE (triangle), and OWSI (diamond) sites.

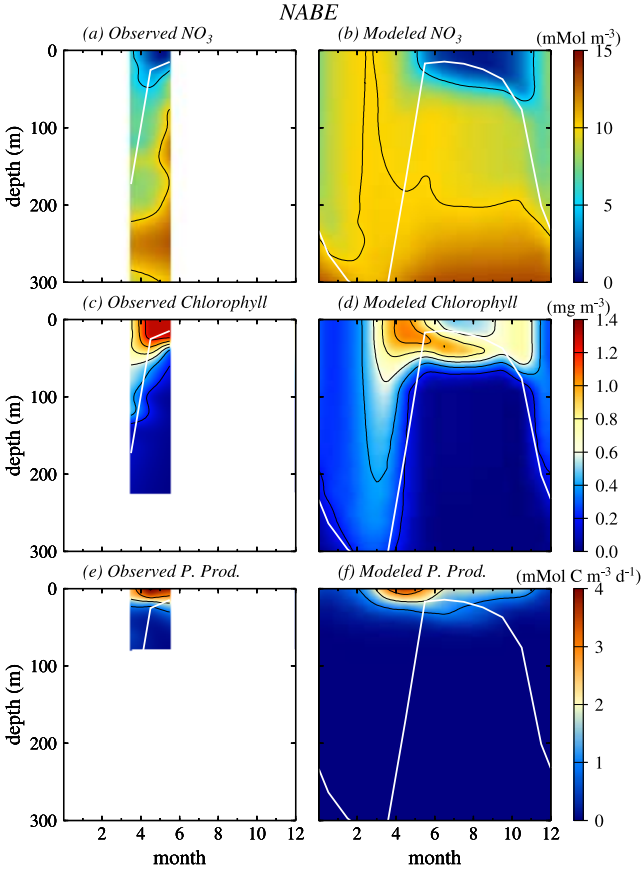

Figure 11. Time series of monthly climatological means of observed and modeled (a and b) NO_3^- (mMol m^{-3}), (c and d) chlorophyll concentrations (mg Chl m^{-3}), and (e and f) primary production (mMol C m^{-3} d^{-1}) at the NABE site. White line represents mixed layer depth.

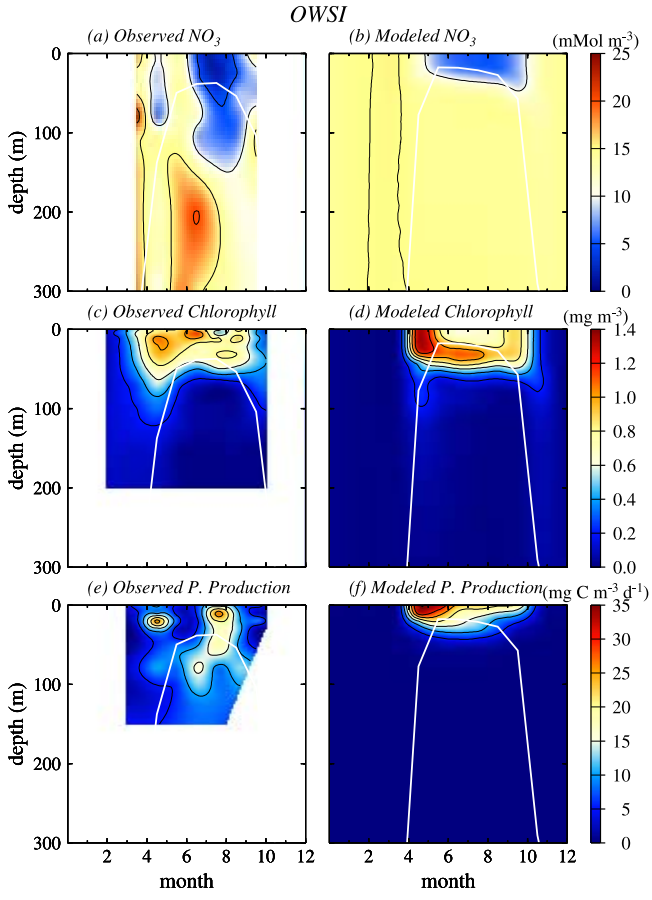

Figure 12. Time series of monthly climatological means of observed and modeled (a and b) NO_3^- (mMol m^{-3}), (c and d) chlorophyll concentrations (mg Chl m^{-3}), and (e and f) primary production (mg C m^{-3} d^{-1}) at the OWSI site. White line represents mixed layer depth.

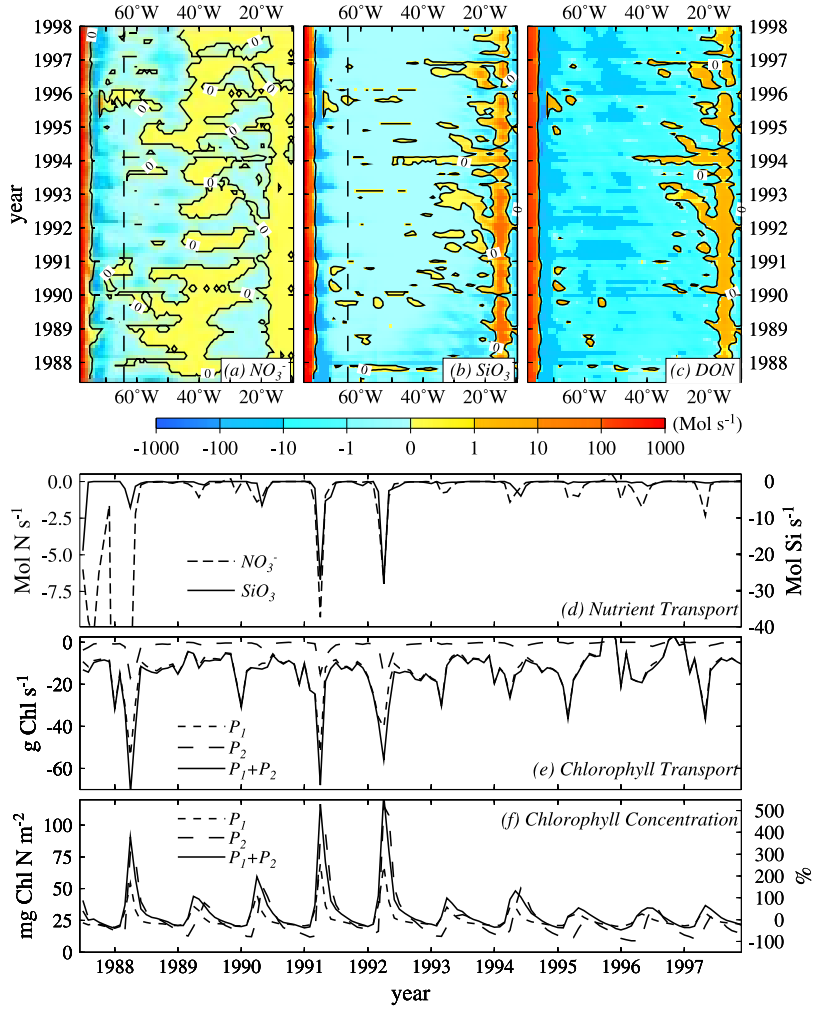

Figure 14. Time series of the meridional transport (Mol s^{-1}) of (a) NO_3^-, (b) SiO_3, and (c) dissolved organic carbon (DON) in the top 107 m across 31°32′N (around the BATS site). The dashed lines in Figures 14a and 14b correspond to the longitude of the BATS site and (d) the nutrient transport time series plot. (e) Time series of the meridional transport of picophytoplankton and diatom chlorophyll at the same location. Positive and negative values indicate northward and southward transport, respectively. (f) Time series of monthly means of total vertically integrated chlorophyll (P_1 + P_2) concentrations (mg m^{-2}) and the percentage change in picophytoplankton (P_1) and diatom (P_2) chlorophyll concentrations in relation to their respective means.

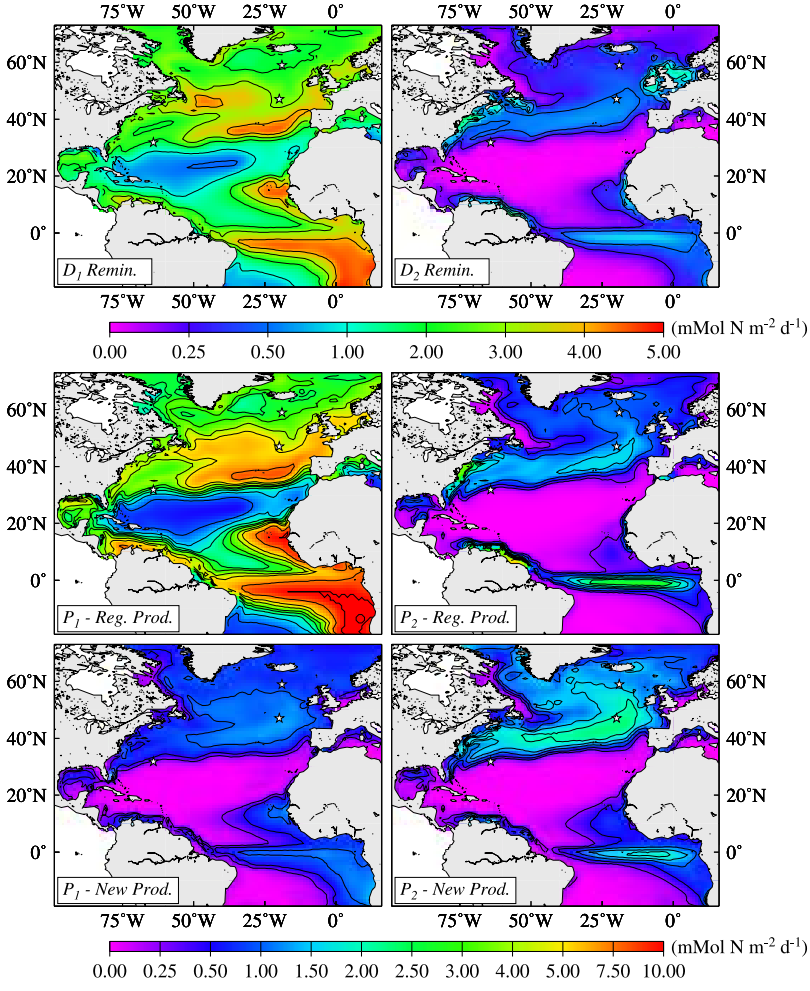

Figure 15. Annual mean distribution of vertically integrated suspended (D_1) and sinking (D_2) detritus remineralization (mMol N m^{-2} d^{-1}) and new and regenerated production by the picophytoplankton (P_1) and diatoms (P_2) (mMol N m^{-2} d^{-1}).